

ANALYSIS OF A STATE CHANGING SUPERSOFT X-RAY SOURCE IN M31

B. Patel¹, R. Di Stefano², T. Nelson³, F. A. Primini², J. Liu², S. Scoles²

ABSTRACT

We report on observations of a SSS in M31, r1-25, that has exhibited spectral changes to harder X-ray states. We document these spectral changes. In addition, we show that they have important implications for modeling the source. Quasisoft states in a source that has been observed as an SSS represent a newly-discovered phenomenon. We show how such state changers could prove to be examples of unusual black hole or neutron star accretors. Future observations of this and other state changers can provide the information needed to determine the nature(s) of these intriguing new sources.

Subject headings: galaxies: individual (M31) – X-rays: binaries

1. INTRODUCTION

Luminous supersoft X-ray sources (SSSs) were established as a class by Einstein Observatory observations of roughly 30 sources in the Magellanic Clouds, Milky Way, and M31 (Greiner 2000). *Chandra* and *XMM-Newton* observations of external galaxies have now discovered hundreds of soft X-ray sources with properties that both exemplify and extend the class of SSSs (e.g., Orio et al. 2010, references therein). Even though they are bright, with luminosities higher than 10^{36} ergs s⁻¹, we know of only a handful in the Galaxy, because the radiation they emit is readily absorbed by the interstellar medium. In fact, the SSSs used to define the class display little or no emission above 1 keV. Roughly a dozen SSSs are known in the Magellanic Clouds (Greiner 2000). Some of these are associated with novae, and are clearly hot white dwarfs (see Greiner 2000). In M31, SSSs have been shown to be associated with supernova remnants, novae, and active galactic nuclei (Orio et al. 2010).

¹Department of Physics and Astronomy, Rutgers, The State University of New Jersey, Piscataway, NJ 08854-8019

²Harvard-Smithsonian Center for Astrophysics, 60 Garden st. Cambridge, MA 02138

³Department of Physics, 1000 Hilltop Circle, University of Maryland at Baltimore, Baltimore, MD 21250

The more mysterious component of the class is comprised of X-ray binaries, most with orbital periods of a day or less. A promising model for these sources is one in which their prodigious luminosities are produced by the nuclear burning of matter accreted by a white dwarf (van den Heuvel et al. 1992; Rappaport et al. 1994; Hachisu et al. 1996; Di Stefano & Nelson 1996). Nuclear burning should allow the white dwarf to retain accreted matter and increase in mass. Binary SSSs have therefore been suggested as progenitors of accretion-induced collapse (van den Heuvel et al. 1992) and of Type Ia supernovae (Rappaport et al. 1994). Nuclear-burning white dwarfs in wider orbits are also expected. Indeed, symbiotic binaries have been observed as SSSs (e.g., Greiner 2000; Orio et al. 2007).

Because it is difficult to detect SSSs in the Milky Way, and the Magellanic Clouds are too small to host a large population, it is important to search for SSSs in external galaxies. The advent of *Chandra* and *XMM-Newton* has made such searches possible. Hundreds of SSSs have now been discovered, some in galaxies as far from us as the Virgo cluster (Liu 2008). As the numbers of SSSs has increased, we have begun to find evidence of sources that have properties different from those of the SSSs that established the class. Some SSSs are hundreds of times more luminous than the Eddington limit for a Chandrasekhar-mass white dwarf. Several of these ultraluminous supersoft sources are candidates for accreting black holes (Di Stefano et al. 2004). In addition, the search for the softest sources has identified a class of sources that are significantly harder than SSSs, yet also significantly softer than canonical X-ray sources. Quasisoft X-ray sources have luminosities above 10^{36} ergs s $^{-1}$, but emit few or no photons with energy above 2 keV (Di Stefano et al. 2004). Some could be hot white dwarfs in which there is an additional hard component and/or which are highly absorbed. Those fitting this model are good candidates for progenitors of Type Ia supernovae, because they would likely correspond to the most massive nuclear-burning white dwarfs (e.g., Rappaport et al. 1994; Di Stefano 2010, references). Others are too hot to be white dwarfs and may correspond to either black holes or neutron stars.

In this paper we report on a source (r1-25) that has been observed to switch between SSS and QSS states (Stiele et al. 2008, 2010; Di Stefano et al. 2010; Orio et al. 2010). No such sources are known in the Galaxy or Magellanic Clouds. We examined all available *Chandra* and *Swift* data and optical data from HST and from the Local Group survey. We also checked the literature for *XMM-Newton* observations and analysis of the source. The question we want to answer is: what is the physical nature of this unique source?

We analyze the X-ray and optical data for the source in §2 and §4, respectively. In §3, we present evidence that the source changes state. We discuss the possible models that fit this source in §5.

2. X-ray Observations and Analysis

The state changing source r1-25 has been reported on multiple times (Kong et al. 2002; Williams et al. 2004; Di Stefano et al. 2004; Kaaret 2002; Voss & Gilfanov 2007; Stiele et al. 2010; Di Stefano et al. 2010; Orio et al. 2010). It is located in the central region of M31 approximately $0.4'$ from the nucleus. The coordinates of the source are (J2000.0) RA = 00:42:47.90, DEC = +41:15:49.99 (see §4 to see how it was calculated). This region of M31 has been well sampled over the past 11 years. In this paper, we searched the *Chandra* archive for all public observations of r1-25 through June 2, 2009. The observations that covered the source are shown in Table 1 and include 86 observations. r1-25 was detected in 45 observations (28 ACIS-I, 2 ACIS-S, and 15 HRC-I observations) from August 8, 2000 to March 11, 2009. We note that the source position was the same in all detections, and we are confident that r1-25 is one source (see Figure 1). We supplemented the *Chandra* data with *Swift* observations of the region in 2009. However, the source was off during the *Swift* observations and are not included in this paper.

We took photometry results from Liu (2008) for observations listed in that paper. We photometered the recent ACIS data in the same manner as Liu (2008). We used CIAO version 4.1.2 (Fruscione et al. 2006) to analyze the recent data. For source detection, we used CIAO tool `wavdetect` (Freeman et al. 2002; Fruscione et al. 2006). We set the scales for `wavdetect` to $1''$, $2''$, $4''$, and $8''$. The chance detection threshold was set to 10^{-6} . The source aperture size was defined as the 3σ elliptical source region computed by `wavdetect`. The background aperture was defined as an elliptical annulus around the source region. The annulus had radii of two and four times the source ellipse radius. Since the source is not near any other X-ray sources, the background aperture size was suitable for all ACIS observations.

Only photons between 0.1-7 keV were considered and the following bands were used to classify them: Soft, 0.1-1.1 keV; Medium, 1.1-2 keV; and Hard, 2-7 keV. The counts in each band and the total for the source were computed as $C_s - C_b \times A_s/A_b$, and the uncertainty was computed as $1 + \sqrt{0.75 + C_s + C_b \times (A_s/A_b)^2}$, with C_s as the counts in the source aperture, A_s as the source aperture area, C_b as the counts in the background aperture, and A_b as the background aperture area. The total count rate, as well as the rate in each band, were corrected by a vignetting factor. The vignetting factor was derived from the exposure map as the ratio between the local and the maximum map value.

For HRC-I observations, we used the CIAO tool `dmextract` (Fruscione et al. 2006) to extract raw counts in source and background apertures, as shown in Figure 2, and to compute net counts. We defined aperture sizes so that the source aperture encircled energy fraction was ~ 1 and the background aperture fraction 0. We also used the CIAO `aprates` (Fruscione et al. 2006) tool to compute the background-marginalized posterior probability

distribution for the source rates, assuming non-informative prior distributions for source and background rates (Kashyap et al. 2009). We note that the HRC data were not corrected for vignetting. Thus, the rates are lower than the ACIS counterparts by 10% or less.

For sources with low flux significance, defined as $netrate/\sigma_{netrate} < 3$, we used the posterior probability distributions to estimate the 3σ upper limits to the rate. The upper limits were calculated using `aprates`. The same method was applied to both HRC and ACIS observations to determine upper limits. For ObsID 10552, there were no counts in the source or background apertures. We could not calculate upper limits for this observation.

Table 2 shows the photometry results for r1-25. The first column is the Modified Julian Date (MJD) for each observation. The next three columns are the counts in the Soft, Medium, and Hard bands, respectively. The fourth column is the Total counts for ACIS observations (in the energy range of 0.1-7 keV). The uncertainties are 1σ in magnitude and calculated using Poisson statistics. The next four columns are the Soft Count Rate (SCR), Medium Count Rate (MCR), Hard Count Rate (HCR), and the Total Count Rate (TCR), respectively. The last column of Table 2 is discussed in §3.2.

Figure 3 shows the light curve for r1-25. The top panel shows the count rate in each band (soft, medium, and hard) vs. obsdate, and the middle panel shows the total counts (in ACIS observations) vs. Obsdate. The top panel demonstrates that the relative count rates change over time for the source. The middle panel indicates that the source alternates between being dominated by soft and medium photons. The bottom panel of Figure 3 is discussed in §3.2

3. Evidence for State Change

3.1. XSPEC

We used the CIAO tool `dmextract` to create source spectra for all observations where more than 60 source counts were collected. These were ObsIDs 1575 (ACIS-S, 183 source counts), 4720 (ACIS-I, 61 source counts), 4721 (ACIS-I, 65 source counts), and 4722 (ACIS-I, 62 source counts). Source spectra were extracted from a circular region with radius 6 pixels centered on the source. Associated background spectra were extracted from an annular region (also centered on the source) with inner and outer radii of 10 and 25 pixels, respectively. For all observations, we created spectral response files using the CIAO tasks `mkacisrmf` and `mkarf` (Fruscione et al. 2006).

We modeled the resulting spectra using the XSPEC package (Arnaud 1996). Since the

number of source counts is rather small, we chose to fit the unbinned spectra using the C -statistic (Cash 1979) rather than the χ^2 statistic, which has been shown to introduce a systematic bias in parameter estimation in low count rate spectra. One caveat in using the C -statistic is that the background is negligible within the source extraction region. This is definitely the case in our ACIS-I observations (~ 1 background count expected in the source region), and an acceptable approximation in the ACIS-S observation of r1-25 (only 17 background counts). The C -statistic as implemented in XSPEC does not provide a measurement of the goodness of fit, but can be used to constrain parameter confidence intervals, which we have done here.

We fit a simple absorbed blackbody model to each spectrum in the energy range 0.3–8.0 keV, using the wabs model for the interstellar absorption (Morrison & McCammon 1983). None of the spectra had enough counts below 1 keV to place a tight constraint on the interstellar column density (in several cases the fits were consistent with no absorption), so we fixed N_H at two values representative of the range expected towards an X-ray source in M31 (1.1×10^{21} and $6.4 \times 10^{21} \text{ cm}^{-2}$). The lower limit was taken from Di Stefano et al. (2004). The upper limit is shown for completeness; it is very unlikely that the source has such a large column density. The resulting parameter values and their 1σ uncertainties are presented in Table 3. We note that our results for ObsID 1575 (we found $0.120 \text{ keV} < kT < 0.140$) are consistent with those reported in Di Stefano et al. (2004) (they found that $kT = 0.122 \text{ keV}$). Examining the temperatures found for r1-25, a clear increase in the later observations can be seen, independent of the choice of absorbing column. At the 90% confidence level, the temperature found for the ACIS-S spectrum is $\sim 0.1 \text{ keV}$ lower than the ACIS-I values. The blackbody temperature returned by the model fitting is constrained primarily by the high energy cut off. Although ACIS-I has poorer low energy sensitivity, the fact that significantly harder counts are detected in such short exposures indicates that the increase in model temperature is real and independent of the differences between the two ACIS instruments.

In order to assess the statistical significance of our observed state changes, we used the simulation capabilities of the spectral fitting package XSPEC (Arnaud 1996). In observation 1575 (a 38 ks ACIS-S observation), 183 counts were detected for the source and we derived two best fit thermal models (depending on assumed N_H , see Table 4) with $kT = 0.08$ or 0.13 keV . Later, in observations 4720, 4721 and 4722 (three 4 ks ACIS-I observations), approximately 60 counts were detected in each, and the derived temperatures were in the range 0.15–0.27 keV. We want to determine the likelihood that, given the differences in instrumental response and exposure time, the best fit model from ObsID 1575 produces the observed counts distribution in ObsIDs 4720–4722.

We used the `fakeit` command in XSPEC to simulate 1000 observations, using the best fit model from ObsID 1575 as input, and the appropriate response files and exposure time for the location of r1-25 in each of the ACIS-I observations. For each simulation, we recorded the counts in each of the energy bands outlined in §2, and then used the ensemble of simulations to determine the associated error. Finally, we compared this to the observed counts distribution.

Our results are recorded in Table 4. It is clear that the softer best fit model found for observation 1575 cannot account for the observed counts distribution in observations 4720–4722: such a source is simply too soft to give rise to the required counts above 1 keV. The same is true when considering the opposite situation—the best fit models derived for the harder state would produce a much larger number of counts in the ACIS-S band than observed, primarily because of the long duration of that particular observation. Looking at Table 4, the observed counts in all cases differ from the tested model by a significant margin (up to 20σ). Therefore, we can state with confidence that the source experienced a real transition from a softer state to a harder one.

3.2. Spectral Estimates from `pimms`

For the majority of ACIS detections of r1-25, there were fewer than 60 total counts. We found that using a spectral fitting program was not a viable option for these observations. Instead, we used HEASARC tool `pimms` (Mukai 1993) included in the CIAO package to estimate the appropriate spectral models. For cycles *Chandra* A01 and A02, we had to create effective area maps, as `pimms` no longer provides support for these cycles. The maps were created by running CIAO tool `mkarf` (Fruscione et al. 2006) for on-axis sources in both cycles (note, `mkarf` was not run on r1-25, but for other X-ray sources that were on-axis). The process was completed for the ACIS-I, ACIS-S, and HRC-I instruments. Effective area maps created by `mkarf` differ slightly from the default `pimms` maps because they are created for specific observations. However, the different effective area maps produce similar spectral estimates, which we discuss later in the section.

The method we used is similar to the Di Stefano et al. (2004) approach. The process compares the observed $\frac{SCR}{TCR}$, $\frac{MCR}{TCR}$, and $\frac{HCR}{TCR}$ to the same ratios calculated by `pimms` for different spectral models (we call the `pimms` ratios $\frac{SCR_p}{TCR_p}$, $\frac{MCR_p}{TCR_p}$, and $\frac{HCR_p}{TCR_p}$). If the `pimms` ratios are within the 1σ uncertainty range for all three of the observed ratios, the model is a match. We used the same set of inputs for all ACIS observations that detected the source. Our XSPEC analysis suggested that black bodies fit the data well. So, we used a black body model to fit the data using `pimms`. The black body kT input was varied from 0.025 to 1.224

keV. We assumed an $N_H = 1.1 \times 10^{21} \text{ cm}^{-2}$. We input an unabsorbed X-ray flux (0.1-7 keV) corresponding to $L_X = 10^{39} \text{ ergs s}^{-1}$. This value was simply an initial guess for the L_X ; the guess was incorrect for the observations. However, we corrected the X-ray luminosity (calling it the $L_{X,p}$) using the ratio of the TCR and TCRp. That is:

$$L_{X,p} = \frac{TCR}{TCRp} \times 10^{39} \text{ ergs s}^{-1} \quad (1)$$

Table 5 shows an example of the **pimms** method for ACIS-S observation 1854 (OBSMJD 51922.4). The first column is the kT (in keV) that was input. The next three columns show the ratios for the $\frac{SCRp}{TCRp}$, $\frac{MCRp}{TCRp}$, and $\frac{HCRp}{TCRp}$, respectively. The last column shows the value of L_X for each value of kT , and were calculated using equation (1). The ratios in the table were compared to the observed ones (the values of kT that fit the observation are in bold in Table 5). The range for the observed ratios were:

$$\begin{aligned} 0.626 &< \frac{SCR}{TCR} < 1.12 \\ 2.65 \times 10^{-3} &< \frac{MCR}{TCR} < 0.262 \\ -8.43 \times 10^{-2} &< \frac{HCR}{TCR} < 8.43 \times 10^{-2} \end{aligned}$$

We applied a second step to the method to reduce the range of temperatures that fit each observation. We broke the soft band down into smaller bins, as shown in Table 6, and followed the same procedure as above. That is, we compared the ratios of the observed values and those calculated by **pimms** for these smaller bins. This additional step significantly decreased the range of kT that fit each observation. For example, using just the first step for ObsID 1854 (see Table 6), there were three values of kT that fit (0.083, 0.112 keV, 0.151 keV). After applying the second step, we were able to exclude the two higher values of kT . However, for many observations the kT range was still over 100 eV after applying the second step.

As a test of the **pimms** method, we applied it to the four observations that were analyzed with XSPEC. Table 7 shows a comparison of the fitting results from XSPEC and **pimms** for $N_H = 1.1 \times 10^{21} \text{ cm}^{-2}$. The first two columns are the observation ID and MJD. The third and fourth columns show the kT range determined by XSPEC and **pimms**, respectively. The two methods produce similar results, demonstrating the validity of our **pimms** estimation method.

Table 8 shows the results from the `pimms` method. The XSPEC results are shown in place of the `pimms` estimates for the four observations described in §3.1. The last two columns show the range of kT and L_X that fit each observation. For all observations, the minimum value of kT that fit corresponds to the maximum value of L_X . The table shows clear evidence for state change. This can be better seen in Figure 4, which graphically display the spectra for r1-25. Again, we used the XSPEC (black symbols) results instead of the those from `pimms` (blue symbols) for the four observations analyzed in §3.1. The plots show a change in both state and L_X for the source. The source is observed in a SSS state (at minimum $kT < 100$ eV), and changes to a QSS state (at maximum $kT > 245$). The source also exhibits a change in L_x of ~ 1 magnitude. We note that, like the XSPEC results, increasing the N_H decreases the kT and increases the L_X that fit the data. However, as with the XSPEC results, the change of state observed in the source using the `pimms` method is seen at larger values of N_H . This implies that the state change is not dependent on the value of N_H chosen.

As a check of the default effective area maps used by `pimms`, we created effective area maps for several observations. The effective area maps were created for on-axis sources using `mkarf`. We then recalculated the ratios predicted by `pimms` using the new maps. The ratios calculated from the two methods differed by 0.01 at most. This difference leads to a small change (at most 5 eV) in the range of kT values that fit. This is a negligible change considering the inherent uncertainties associated with using `pimms`. Furthermore, the kT range for most observations was ~ 100 eV (see Table 8). Thus, there would still be evidence for state change if `mkarf` effective area maps were used instead of the default `pimms` maps.

We used the `pimms` estimates to convert ACIS-S and HRC-I count rates to ACIS-I units (see the last column of Table 2, as well as the bottom panel in Figure 3). This calculation is done to compare the results between *Chandra* instruments. We choose ACIS-I units because most of the detections of the source were in this instrument. Thus, the last two columns of Table 2 show the same count rate for ACIS-I observations.

For ACIS-S detections of r1-25, we use `pimms` to convert the total count rate to ACIS-I units using the appropriate spectral models (see Table 8). We ran `pimms` twice to determine the upper and lower bounds of the converted rate. To determine the upper bound, we input the following count rate: $TCR + eTCR$, where $eTCR$ is the uncertainty in total count rate. The model used was the maximum value of kT determined to fit the observation. To determine the lower bound, we input: $TCR - eTCR$, using the minimum value of kT determined to fit the observation as the model. In both calculations, we assumed a $N_H = 1.1 \times 10^{21} \text{ cm}^{-2}$.

HRC-I observations and ACIS-S non-detections of the source provided no spectral information. For these observations, we assumed a spectral model and then applied the same

process as above to convert to an ACIS-I count rate. All observations in *Chandra* cycles A01, A02, and A03 were converted assuming: $0.075 \text{ keV} < kT < 0.200 \text{ keV}$. For the rest, we determined the appropriate range of kT from the first ACIS detections before and after the observation. For example, HRC-I observation 7285 (MJD 54052.3) detected the source. The first ACIS detection preceding it was ObsID 7140 (MJD 54002.8; $0.160 \text{ keV} < kT < 0.205 \text{ keV}$, see Table 8) and the first after was ObsID 7064 (MJD 54073.9; $0.120 \text{ keV} < kT < 0.165 \text{ keV}$, see Table 8). We used the following range for kT for ObsID 7285: $0.120 \text{ keV} < kT < 0.205 \text{ keV}$.

3.3. X-ray Color Ratios

Using the method described in Prestwich et al. (2003), we calculated the soft and hard color ratios for all r1-25 detections with 25 or more counts (the results are shown in Table 9). The ratios were calculated using the following equations for each of the 12 observations in the table:

$$\text{Hard Color Ratio} = \frac{(\text{Hard Counts} - \text{Medium Counts})}{\text{Total Counts}} \quad (2)$$

$$\text{Soft Color Ratio} = \frac{(\text{Medium Counts} - \text{Soft Counts})}{\text{Total Counts}} \quad (3)$$

The color ratios were used to construct a X-ray color-color plot in the same fashion as Prestwich et al. (2003) (see Figure 5). Each area of the plot corresponds to different types of X-ray sources. Figure 5 further demonstrates the strange behavior of this source, as it has detections in very different locations on the graph.

4. Optical Observations and Analysis

The location of r1-25 has been observed with the ACS camera onboard *HST* (see Table 10). In both cases, images are only available in the F435W filter (approximately equal to the *B* filter in ground based systems). We have 4 observations acquired in the period 2004–2007, so the data are useful for looking for transient or variable sources. Only one *Chandra* observation (ObsID 8183) was taken within a week of an ACS observation (j9ju06010) of the source. However, the source was not detected in ObsID 8183.

All data were obtained using the Wide Field Channel (WFC), which has a $202'' \times 202''$ field of view (Maybhate et al. 2010). Each observation was carried out in the standard four pointing dither pattern (Maybhate et al. 2010). These individual images were then combined

using the PyRAF task MultiDrizzle (Fruchter et al. 2009), which also removes cosmic rays and corrects the geometrical distortion which results from the orientation of the ACS with respect to the HST focal plane. We chose not to apply an automatic background subtraction in order to perform photometry, since there is a steep gradient in the diffuse light this close to the center of M31 making background estimation unreliable. Finally, we utilized the ability of MultiDrizzle to resample the spatial scale of the image, resulting in a final pixel scale of $0.025''/\text{pix}$.

The World Coordinate System (WCS) in HST images can be offset from standard reference frames by as much as one arcsecond (Maybath et al. 2010). To improve the astrometry, we registered the final drizzled images to the WCS of the Local Group Survey (LGS) images of M31 (Massey et al. 2006). Stars common to both images were identified, and their centroid positions calculated using the IRAF task `imcentroid`. We then used the task `ccmap` in IRAF to update the WCS of the HST images. The final rms (1σ) errors in the alignment were of order $0.006''$ in RA, and $0.002''$ in declination. We note that the RMS errors on the alignment of the HST images to the WCS of the LGS survey were always smaller than $0.01''$ (which is smaller than one pixel in the rescaled images).

We also aligned the deepest *Chandra* observation (ObsID 1575) with the WCS of the LGS images using the same procedure applied to the HST images. We found an alignment error of $0.109''$ in RA and $0.149''$ in DEC. The centroid position in the corrected WCS for the source is RA:00:42:47.90, DEC:+41:15:49.99, with errors of $0.08''$ (RA) and $0.07''$ (DEC). To get the final positional error, we added the alignment and centroid errors in quadrature. The final RA error is $0.13''$ and final DEC error is $0.17''$ (these are 1σ errors).

Since the WFC images cover such a large area and contain so many stars, we extracted subimages 1000 pixels on a side centered on our source of interest and performed photometry on those. We used the DAOPHOT II and ALLSTAR routines (Stetson et al. 1990) to find and photometer stars in the images. Stars suitable for calculating a point spread functions (PSFs) were identified by hand to avoid problems due to crowding. The final measured counts for each star were converted first to count rate by dividing by the exposure time of each observation, and then to AB system magnitudes using the conversion factors in the ACS users handbook (Maybath et al. 2010).

We show the final reduced image for the source in Figure 6, superimposed with the X-ray 3σ positional error ellipse. The ellipse is drawn using the 3σ RA error ($0.39''$) as the semi-major axis and the 3σ DEC error ($0.51''$) as the semi-minor axis. The location of r1-25 is extremely crowded, and being so close to the core is subject to a high background of diffuse light. In our series of four images, two (j9ju01010 and j9ju06010) are also significantly deeper, which affects the completeness of the stars we can detect. The small size of the Chandra

error circle does however simplify the analysis of the photometry, since very few sources are inside the X-ray 3σ error ellipse. Examining the images, a number of sources are detected inside the error circle, although most are unresolved. We note that there are no catalog stars within the *Chandra* error ellipse. In fact, only one source is resolved inside the error ellipse in all four images by the photometry source detection algorithm. We have marked this source with a red circle in Figure 6.

The single resolved source in Figure 6 has observed magnitudes of 24.45 ± 0.06 , 24.27 ± 0.05 , 24.31 ± 0.04 and 24.41 ± 0.04 in each of the four images, where the quoted error is the 1σ magnitude error. Using the standard $E(B-V) = 0.062$ for M31 (Schlegel et al. 1998), the extinction in the F435W filter is 0.785 magnitudes. Thus, the star’s M_B is between -0.80 and -0.98 in the four observations, assuming $(m-M)_0 = 24.47$ (Holland 1998). This demonstrates that, within the uncertainties, there is no evidence of variability in this object. Although other sources are picked up by the DAOphot detection algorithm inside the error ellipse in some images, these additional detections can be accounted for by the longer exposure time, or are unreliable due to crowding.

(Grupe et al. 2010) looked at the spectral energy distribution of 92 active galactic nuclei that had soft X-ray spectra. The AGN they studied had comparable X-ray count rates to r1-25. However, the AGN were much brighter in the B band ($14 < m_B < 18$) than any source in Figure 6. For this reason, we are confident that r1-25 is not an AGN.

With no color information, we cannot determine what the object marked in Figure 6 is for certain. If it is a star, it would correspond to a late B type with bolometric luminosity of 10^{36} ergs s^{-1} . We note that it is too luminous in the B band to be a red giant, and too dim to be a red supergiant.

5. Models

The state changes observed in r1-25 are extremely unusual for a SSS, and quite different than state changes observed in other classes of X-ray source. In this section, we consider a number of physical models with the goal of uncovering the nature of the X-ray emitting source. In order for any model of r1-25 to be successful, it must be able to explain all of the observed features of the source. These features include the source’s appearance as an SSS-HR source in observation 1575 with ACIS-S, with $kT \sim 130$ eV and a 0.3–8 keV luminosity of 4×10^{36} erg s^{-1} . We wish to emphasize once again that even though r1-25 had an effective temperature in excess of 100 eV when detected as an SSS (much higher than most SSSs), it satisfied the strictest SSS criterion as defined in Di Stefano et al. (2004). That is, the

detection in observation 1575 (when the source was an SSS) had no hard counts, medium counts consistent with zero, and a 3σ detection in the soft band.

Furthermore, the model must explain the subsequent detections of the source as a ~ 250 eV source, *with higher luminosity* than in the soft state ($\sim 10^{37}$ erg s $^{-1}$). Lastly, the model must be consistent with an optical counterpart with F435W magnitude fainter than ~ 24.3 (M_B fainter than ~ -1). We note that white dwarf, neutron star, and black hole SSSs are consistent with this optical restraint. CAL 87, with $M_B \sim 0.5$ (e.g., Greiner 2000; Deutsch et al. 1996), is thought to be a stellar-mass black hole system (e.g., Cowley et al. 1990). RX J0720.4-3125, an isolated neutron star SSS, has a $M_B \sim 18$ (Kaplan et al. 2007, references therein). RX J0439.8-6809, a white dwarf SSS, has a $M_B \sim 2.7$, which is also consistent with the optical constraint on r1-25.

The following subsections outline white dwarf, neutron star and black hole models, and compare their features to the observed properties of r1-25.

5.1. White Dwarfs

White dwarfs that have recently experienced novae have temperatures and luminosities that can make them detectable as SSSs.¹ Many SSSs detected in M31 were recent novae (e.g., Pietsch et al. 2005, 2007; Stiele et al. 2010, references therein). When the white dwarf cools, some novae are detected as harder X-ray sources, but the X-ray luminosity is around $10^{32} - 10^{33}$ ergs s $^{-1}$ (Sala et al. 2010). In contrast, novae in a supersoft state are detected with $kT \sim 50$ eV and L_X of $10^{37} - 10^{38}$ ergs s $^{-1}$ (e.g., Stiele et al. 2010, references therein). Thus r1-25, even in its softest state (with $kT \sim 130$ eV and L_X of 4×10^{36} erg s $^{-1}$), is too hard to be consistent with the very soft emission detected in typical supersoft novae. Also, the source is not consistent with the harder states of novae. That is r1-25, even in its hardest state (~ 250 eV and L_X of 1.1×10^{37} erg s $^{-1}$) is softer and more luminous than novae in their hardest states. Moreover, the harder states of r1-25 are more luminous than the softer ones, in contradiction to what happens in novae. We therefore turn to models in which a white dwarf accretes matter at high rates.

When a white dwarf accretes mass at a high enough rate that the incoming matter can experience nuclear burning, the white dwarf can appear as an SSS. In this case, the source

¹A specific post-nova system will be detectable as an SSS only if the white dwarf stays hot enough to be emitting as an SSS until after the optical depth has decreased enough to let radiation escape (e.g., Sala & Hernanz 2005).

will not be in a hard state. The copious energy we receive from such sources is provided by nuclear burning, rather than accretion. The effective radii are comparable to the white dwarf radii, so the emission can be characterized by values of kT in the range of tens of eV for low-mass white dwarfs, and ~ 100 eV for white dwarfs approaching the Chandrasekhar mass (M_C). For each white dwarf mass, nuclear burning can occur only within a narrow range of accretion rates (Di Stefano 2010). These rates are very high: $\sim 10^{-7} M_\odot$ for a solar-mass white dwarf, ten times higher for a white dwarf with mass near M_C (Di Stefano 2010). At such rates of infall, accretion alone produces luminosities in the range of $10^{36} - 10^{37}$ ergs s $^{-1}$, typically a few percent of the total energy of the system.

Consider a case, when its accretion rate places a white dwarf near the lower end of the steady-burning region, or just below it. In this case, nuclear burning may be episodic. During and just after nuclear-burning episodes, the emission is dominated by soft emission. As the white dwarf cools, however, it becomes less luminous and the emission is dominated by accretion. Although at high rates of accretion, the emission is expected to be softer than typical for low-accretion-rate white dwarfs, such as cataclysmic variables, it can nevertheless be harder than typical of SSSs (e.g., Popham & Narayan 1995; Patterson & Raymond 1985). Thus, the source could appear to be quasisoft or hard. If the donor is a giant or a Roche-lobe filling star in a circular orbit, the accretion rate should could continue to be high. The source will continue to be detected as a harder source. Nuclear burning episodes occurring at intervals ranging from months to decades would make the source more luminous and detectable as an SSS.

The points made above about the quasi-steady nuclear burning white dwarf model are illustrated in Figure 7. The figure is a plot of kT vs. the logarithm of bolometric luminosity, LOG[L] for various quasi-steady nuclear burning white dwarfs (green points) along with the r1-25 spectra (black, blue, and red points). The solid and open black points represent the XSPEC spectral fits of r1-25. The solid black points represent the fits where we assume $L_X = L$. The X-ray luminosity, however, is not equivalent to the bolometric luminosity. We assume that the X-ray luminosity represents, at a minimum, a quarter of the bolometric luminosity. Thus, we plot the open black circles which represent XSPEC fits assuming $L_X = 0.25L$. The solid blue points, which represent the spectral fits for observations with fewer counts (spectra estimated using the `pimms` method described in §3.2), are included for completeness. They represent the `pimms` spectral estimates assuming $L_X = L$. The red points represent the `pimms` results assuming $L_X = 0.25L$. However, as noted in §3.2, these spectral fits are estimates. For this reason, we point out that the XSPEC results are more reliable. In fact, the error bars are so large for the `pimms` results that they cover most of the plot. The `pimms` uncertainties are excluded for this reason. The plot clearly indicates that the quasi-steady nuclear burning white dwarf model does not fit r1-25, as the data are

to hard and/or dim to fit the model. That is, no XSPEC points and only one of the `pimms` points fall in the range of quasi-steady nuclear burning.

5.2. Neutron Stars

Isolated neutron stars and neutron stars in quiescent low-mass X-ray binaries (qLMXBs) have been observed with spectra in the SSS or QSS range, but they are typically 3-5 orders of magnitude less luminous than the “classical” SSSs and QSSs (e.g., Haberl 2007; Pires et al. 2009). Kylafis & Xilouris (1993) showed, however, that the combination of gravitational and magnetic effects can cause neutron stars accreting near the Eddington limit to produce SSS-like spectra. In such cases, the luminosities and temperatures would give the accreting neutron stars the appearance of “classical” SSSs. Nevertheless, neutron-star models for SSSs have received relatively little attention, perhaps because of the success of white dwarf models, coupled with what appeared to be the fine tuning required for a neutron star to achieve the appropriate effective radius.

It is therefore worth noting that there is observational support for the idea that neutron stars can produce very soft spectra. Hughes (1994) discovered a transient pulsar in the Small Magellanic Cloud that has an unpulsed, highly luminous (near Eddington) soft ~ 35 eV component. If such a system is viewed from an angle at which the hard radiation is not detected, it would have the properties associated with the “classical” SSSs first discovered in the Magellanic Clouds (Long et al. 1981).

Here we point out that the discovery of QSSs provides reasons to revisit neutron star models. Consider a neutron star producing near-Eddington soft emission. If this emission emanates from a nearly spherical photosphere with radius equal to the Alfvén radius, then

$$kT = 104 \text{ eV} \left(\frac{10^{11} \text{ G}}{B_s} \right)^{\frac{2}{7}} \left(\frac{10 \text{ km}}{R_{NS}} \right)^{\frac{6}{7}} \left(\frac{M}{M_\odot} \right)^{\frac{1}{14}} \left(\frac{L}{10^{37} \text{ ergs s}^{-1}} \right)^{\frac{11}{28}} \quad (4)$$

In this expression, R_{NS} is the radius of the neutron star, B_s is the value of magnetic field on the surface, and M and L represent the neutron star’s mass and luminosity, respectively.

An interesting feature of this expression is that there are ranges of reasonable values of the physical parameters in which the kT is in the range expected for SSSs or QSSs. Furthermore, for a specific neutron star, the effective temperature depends on L which can change as the accretion rate changes. Since changes in accretion rate are common, we may therefore expect the effective temperatures of some neutron stars to change. Depending on the physical parameters, these changes could produce transitions from SSS to QSS states.

Another set of factors support neutron star models for some QSSs and state-changing QSSs. This is that, if there is luminous soft emission, there must also be a hard component generated by matter accreting, which is channeled onto the poles by the neutron star’s strong magnetic field. The hard emission is likely to be beamed. This model therefore predicts that a large population of accreting neutron stars will contain some with a pulsed hard component. If this component is not the dominant one, then the neutron star may appear as a QSS, even if emission from the Alfvén sphere is SSS. The diagnostic for the neutron star model would be periodicity in the arrival times of the harder photons.

Figure 8 shows two plots of kT vs. $\text{LOG}[L]$. The top panel shows several curves for various neutron star models. Each curve differs by a factor of ten in B_s . The bottom plot is of the r1-25 spectra along with the $B_s = 10^{10}$ G curve. The black (XSPEC) and blue (**pimms**) points were plotted in the same manner as in Figure 7 (see §5.1), except that we assumed for neutron star models $L_X \approx L$ only. The distribution of points is roughly consistent with what is expected for this neutron star model. The XSPEC points seem to follow the same trend as the curve, with some variation. There is more variability in the **pimms** data, but the uncertainties are large for these spectral estimates.

It is important to note that if we can identify QSSs and state changers in the Milky Way or in the Magellanic Clouds, then neutron star models are testable. The reason is that neutron stars produce pulsed radiation and/or hard bursts. This is how we have verified the neutron-star natures of LMXBs in the Galaxy’s globular clusters. Both bursts (e.g., Lewin et al. 1993) and pulsed (e.g., Zhelezniakov 1981) radiation would be detectable in nearby neutron stars, even if the radiation is dominated by an unpulsed soft component.

5.3. Black Holes

Accreting black holes can exhibit thermal-dominant states in which the emission is dominated by a component emanating from the inner portion of the accretion disk (e.g., Remillard & McClintock 2006). SSSs and QSSs have therefore both been suggested as possible black holes. In fact, the most well-known state changer is M101-ULX-1, an ultraluminous SSS that has been detected also in high QSS and low-hard states (e.g., Kong et al. 2004; Kong & Di Stefano 2005; Mukai et al. 2005). M101-ULX-1 is almost certainly a black hole. Its mass could be either in the range typical of Galactic stellar-mass black holes or else in the higher range ($50 - 10^4 M_\odot$) suggested for intermediate-mass black holes.

The luminosity of r1-25 is 1-3 orders of magnitude smaller than the luminosities measured for M101-ULX-1 when it is in a soft state. It is therefore highly unlikely to be an

intermediate-mass black hole. In fact, if the luminosity is less than roughly a percent of the Eddington luminosity, then the inner disk will not be optically thick and the emission will not be thermal. This suggests that, if this source is a black hole, it is more likely to be of stellar mass. The top panel of Figure 9, first shown in Di Stefano et al. (2010), shows that QSS emission is expected in the thermal-dominant state of black holes with mass below $\sim 100 M_{\odot}$. The radius of the inner disk would determine the value of the effective temperatures; the spectrum could be either QSS or SSS. At lower rates of accretion, the emission would be hard.

The bottom panel of Figure 9 shows the r1-25 spectra along with the $10M_{\odot}$ and $100M_{\odot}$ curves. The black (XSPEC) and blue (pimms) points were plotted in the same manner as in Figure 8 (see §5.2). The distribution of the points with XSPEC fits is roughly consistent with what is expected for a black hole of roughly $10M_{\odot}$. The distribution of points with fewer counts (pimms fits) is broader, but the uncertainties are larger.

6. Conclusion

We have tracked the long-term behavior of the M31 X-ray source r1-25. First observed by ROSAT on 1990-07-24, then by both *Chandra* and *XMM-Newton* and most recently by Swift, r1-25 is one of the best-studied soft X-ray sources. There are 86 public *Chandra* observations of the source through June 2, 2009, with 45 detections. For *XMM-Newton*, there are 26 public observations of the source, with Stiele et al. (2010) reporting detections in only the 2004 data. The detections of the source start in 1999 and continue through 2009.

By doing this we have documented the fact that r1-25 has transitioned from an SSS to a harder, QSS state. In the SSS state its estimated X-ray luminosity is a few times 10^{36} ergs s^{-1} , and the luminosity appears to be higher, but not much over 10^{37} ergs s^{-1} in the harder state. Only one other X-ray source, M101-ULX-1, has well-studied state changes (e.g., Kong et al. 2004; Kong & Di Stefano 2005; Mukai et al. 2005). While M101-ULX-1, which has been observed with X-ray luminosity as high as $10^{40} - 10^{41}$ ergs s^{-1} , is almost certainly a black hole, the nature of r1-25 is more difficult to establish, because its luminosity range is consistent with white dwarf, neutron star, or black hole accretors.

Whatever its nature it is different from anything we have observed. We have shown that the observed behavior is consistent with a black hole accretor with a mass in the $10M_{\odot}$ range. In this case, our observations of r1-25 have all found it to be in a thermal-dominant state. The inner disk radius would have been larger in the SSS state. If r1-25 is a black hole with a mass of approximately $10M_{\odot}$, it could be more luminous in future observations, if

the donor star is able to contribute mass at a higher rate. Should the luminosity approach the Eddington luminosity, the system would be unlikely to remain in the thermal dominant state, and hard emission could be detected. Similarly, if the luminosity falls below $\sim 1\%$ of the Eddington value, the spectrum would likely be hard.

We have also shown that the observed behavior of r1-25 is consistent with a neutron star accretor with $B_s = 10^{10}$ G. We assume that the magnetic field should be constant over the short interval of observations of the source. The model suggests that the harder states are more luminous than the softer ones, which is consistent with the r1-25 spectra. We note that neutron star models are testable if we can find state changers and QSSs in the Milky Way or Magellanic Clouds, as both bursts and pulsed radiation would be detectable in nearby neutron stars..

White dwarf models are the least likely fit for r1-25. The source does not seem to exhibit behavior of a post-nova system, as its spectrum is harder than novae that are SSSs (even when r1-25 is in its soft state). The source is also too luminous and soft to be consistent with novae in there harder states. Furthermore, quasi-steady nuclear burning white dwarf models do not fit the data. We have shown that quasi-steady nuclear burning models can produce both supersoft and quasisoft radiation, but the model is too soft and/or luminous to fit the r1-25 spectra.

We note that there are other state-changing sources in external galaxies.² For example, there are nine state changing sources in nearby spiral galaxy M33. If we study a large enough sample of state-changers, we are likely to find examples of all three (white dwarf, neutron star, and black hole) models. Continued monitoring of these sources will play an important role in testing these models. It is also important to identify QSSs and state-changers in the Magellanic Clouds and Galaxy, where many test of the nature of the accretors can be conducted.

We would like to thank the *Swift* team for approving our ToO request (Target ID: 35336). This research has made use of the NASA/IPAC Extragalactic Database (NED) which is operated by the Jet Propulsion Laboratory, Caltech, under contract with the National Aeronautics and Space Administration. This research was supported by HST Grant AR-10948.01-A-0 and the Smithsonian Institution IR & D award.

²see <http://www.cfa.harvard.edu/~jffiu/> for a list of state changing sources

REFERENCES

- Arnaud, K. A. 1996, *Astronomical Data Analysis Software and Systems V*, 101, 17
- Cash, W. 1979, *ApJ*, 228, 939
- Cowley, A. P., Schmidtke, P. C., Crampton, D., & Hutchings, J. B. 1990, *ApJ*, 350, 288
- Di Stefano, R., & Nelson, L. A. 1996, *Supersoft X-Ray Sources*, 472, 3
- Di Stefano, R., Kong, A. K. H., Greiner, J., Primini, F. A., Garcia, M. R. et al. 2004, *ApJ*, 610, 247
- Di Stefano, R. 2010, *ApJ*, 712, 728
- Di Stefano, R., Primini, F. A., Liu, J., Kong, A., & Patel, B. 2010, *Astronomische Nachrichten*, 331, 205
- Deutsch, E. W., Margon, B., Wachter, S., & Anderson, S. F. 1996, *ApJ*, 471, 979
- Freeman, P. E., Kashyap, V., Rosner, R., & Lamb, D. Q. 2002, *ApJS*, 138, 185
- Fruchter, A. and Sosey, M. et al. 2009, “The MultiDrizzle Handbook”, Version 3.0 (Baltimore, STScI)
- Fruscione, A., McDowell, J. C., Allen, G. E., Davis, J. E., Durham, N. et al. 2006, *Proc. SPIE*, 6270
- Greiner, J. 2000, *New Astronomy*, 5, 137
- Grupe, D., Komossa, S., Leighly, K. M., & Page, K. L. 2010, *ApJS*, 187, 64
- Haberl, F. 2007, *Ap&SS*, 308, 181
- Hachisu, I., Kato, M., & Nomoto, K. 1996, *ApJ*, 470, L97
- Holland, S. 1998, *AJ*, 115, 1916
- Hughes, J. P. 1994, *ApJ*, 427, L25
- Kashyap, V., Primini, F. A., Glotfelty, K. J., Anderson, C. S., Bonaventura, N. R. et al. 2009, *Bulletin of the American Astronomical Society*, 41, 425
- Kylafis, N. D., & Xilouris, E. M. 1993, *A&A*, 278, L43

- Kong, A. K. H., Garcia, M. R., Primini, F. A., Murray, S. S., Di Stefano, R. et al. 2002, *ApJ*, 577, 738
- Kong, A. K. H., Di Stefano, R., & Yuan, F. 2004, *ApJ*, 617, L49
- Kong, A. K. H., & Di Stefano, R. 2005, *ApJ*, 632, L107
- Kaaret, P. 2002, *ApJ*, 578, 114
- Kaplan, D. L., van Kerkwijk, M. H., & Anderson, J. 2007, *ApJ*, 660, 1428
- Lewin, W. H. G., van Paradijs, J., & Taam, R. E. 1993, *Space Science Reviews*, 62, 223
- Liu, J. 2008, arXiv:0811.0804
- Long, K. S., Helfand, D. J., & Grabelsky, D. A. 1981, *ApJ*, 248, 925
- Massey, P., Olsen, K. A. G., Hodge, P. W., Strong, S. B., Jacoby, G. H. et al. 2006, *AJ*, 131, 2478
- Maybhate, A. et al. 2010, "ACS Instrument Handbook", Version 9.0
- Morrison, R., & McCammon, D. 1983, *ApJ*, 270, 119
- Mukai, K. 1993, *Legacy*, 3, 21
- Mukai, K., Still, M., Corbet, R. H. D., Kuntz, K. D., & Barnard, R. 2005, *ApJ*, 634, 1085
- Orio, M., Zezas, A., Munari, U., Siviero, A., & Tepedelenlioglu, E. 2007, *ApJ*, 661, 1105
- Orio, M., Nelson, T., Bianchini, A., Di Mille, F., & Harbeck, D. 2010, *ApJ*, 717, 739
- Patterson, J., & Raymond, J. C. 1985, *ApJ*, 292, 550
- Pietsch, W., Fliri, J., Freyberg, M. J., Greiner, J., Haberl, F. et al. 2005, *A&A*, 442, 879
- Pietsch, W., Haberl, F., Sala, G., Stiele, H., & Hornoch, K. et al. 2007, *A&A*, 465, 375
- Pires, A. M., Motch, C., Turolla, R., Treves, A., & Popov, S. B. 2009, *A&A*, 498, 233
- Popham, R., & Narayan, R. 1995, *ApJ*, 442, 337
- Prestwich, A. H., Irwin, J. A., Kilgard, R. E., Krauss, M. I., Zezas, A. et al. 2003, *ApJ*, 595, 719
- Rappaport, S., Di Stefano, R., & Smith, J. D. 1994, *ApJ*, 426, 692

- Remillard, R. A., & McClintock, J. E. 2006, *ARA&A*, 44, 49
- Sala, G., & Hernanz, M. 2005, *A&A*, 439, 1061
- Sala, G., Hernanz, M., Ferri, C., & Greiner, J. 2010, *Astronomische Nachrichten*, 331, 201
- Schlegel, D. J., Finkbeiner, D. P., & Davis, M. 1998, *ApJ*, 500, 525
- Stetson, P. B., Davis, L. E., & Crabtree, D. R. 1990, *CCDs in astronomy*, 8, 289
- Stiele, H., Pietsch, W., Haberl, F., & Freyberg, M. 2008, *A&A*, 480, 599
- Stiele, H., Pietsch, W., Haberl, F., Burwitz, V., Hatzidimitriou, D. et al. 2010, *Astronomische Nachrichten*, 331, 212
- van den Heuvel, E. P. J., Bhattacharya, D., Nomoto, K., & Rappaport, S. A. 1992, *A&A*, 262, 97
- Voss, R., & Gilfanov, M. 2007, *A&A*, 468, 49
- Williams, B. F., Garcia, M. R., Kong, A. K. H., Primini, F. A., King, A. R. et al. 2004, *ApJ*, 609, 735
- Zhelezniakov, V. V. 1981, *Ap&SS*, 77, 279

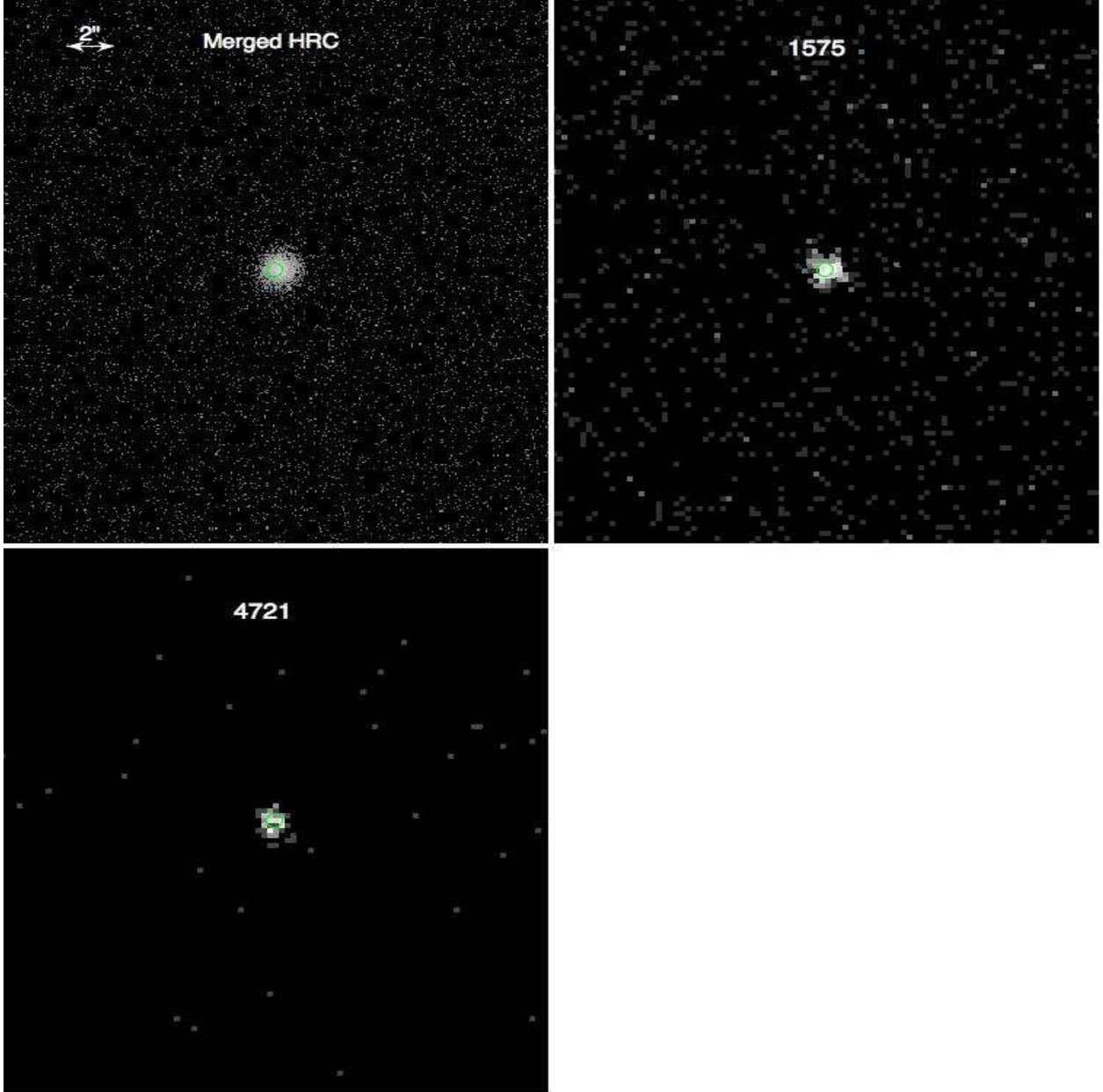


Fig. 1.—: The figure shows the location of r1-25 (the green circle) in M31 in different observations of r1-25. *Top Left*: Merged HRC data of the source. *Top Right*: ACIS-S ObsID 1575 of the source. *Bottom*: ACIS-I ObsID 4721 of the source. The location of the source is the same in the two ACIS observations. Although the HRC data do show an offset of $\sim 0.5''$ from the r1-25 ACIS position, other sources in the field do as well. Thus, the offset comes from a shift in the coordinate frame.

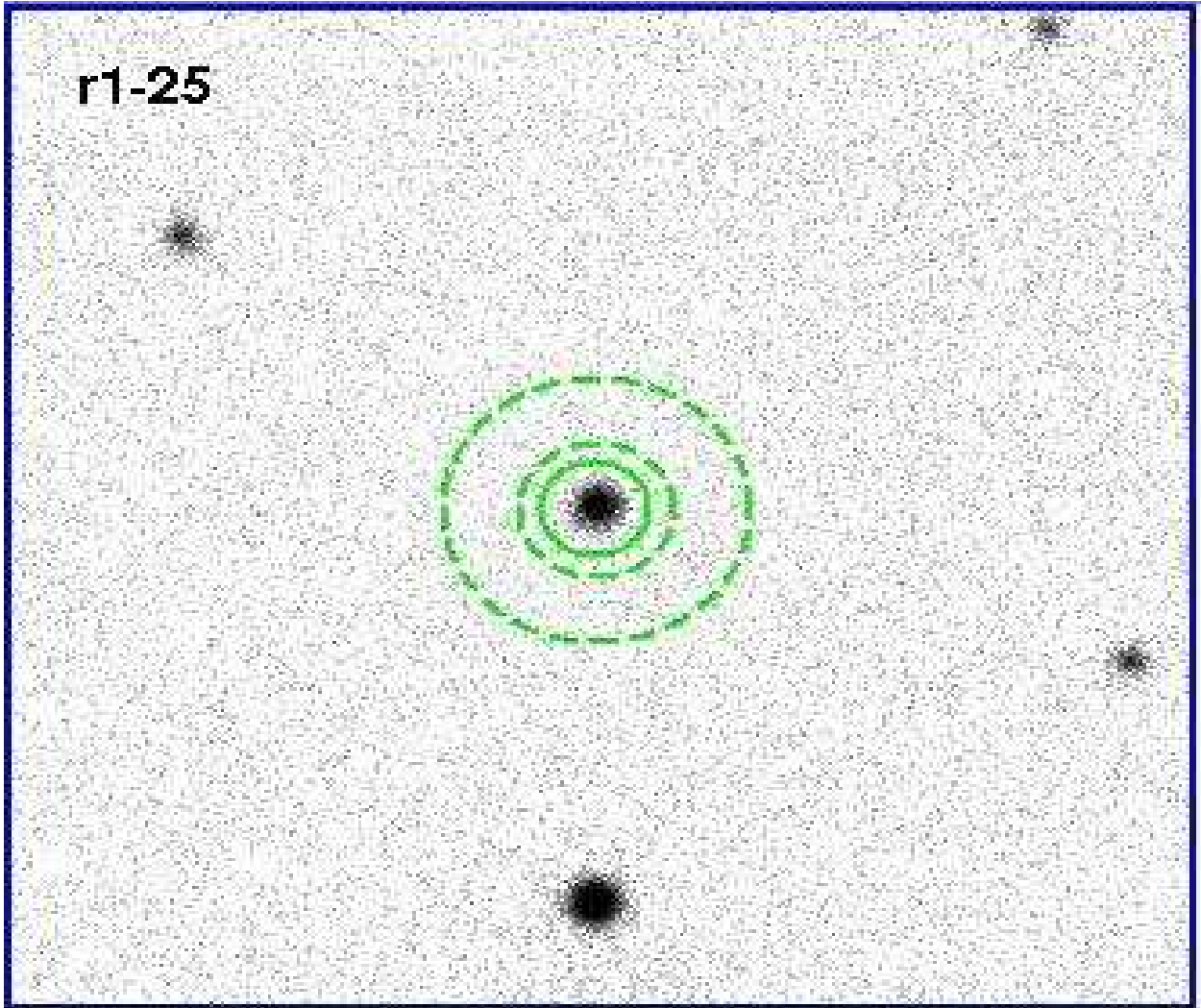


Fig. 2.—: Source (solid) and background (dashed) apertures for r1-25, displayed on a ~ 432 kilosecond merged Chandra HRC-I observation of M31.

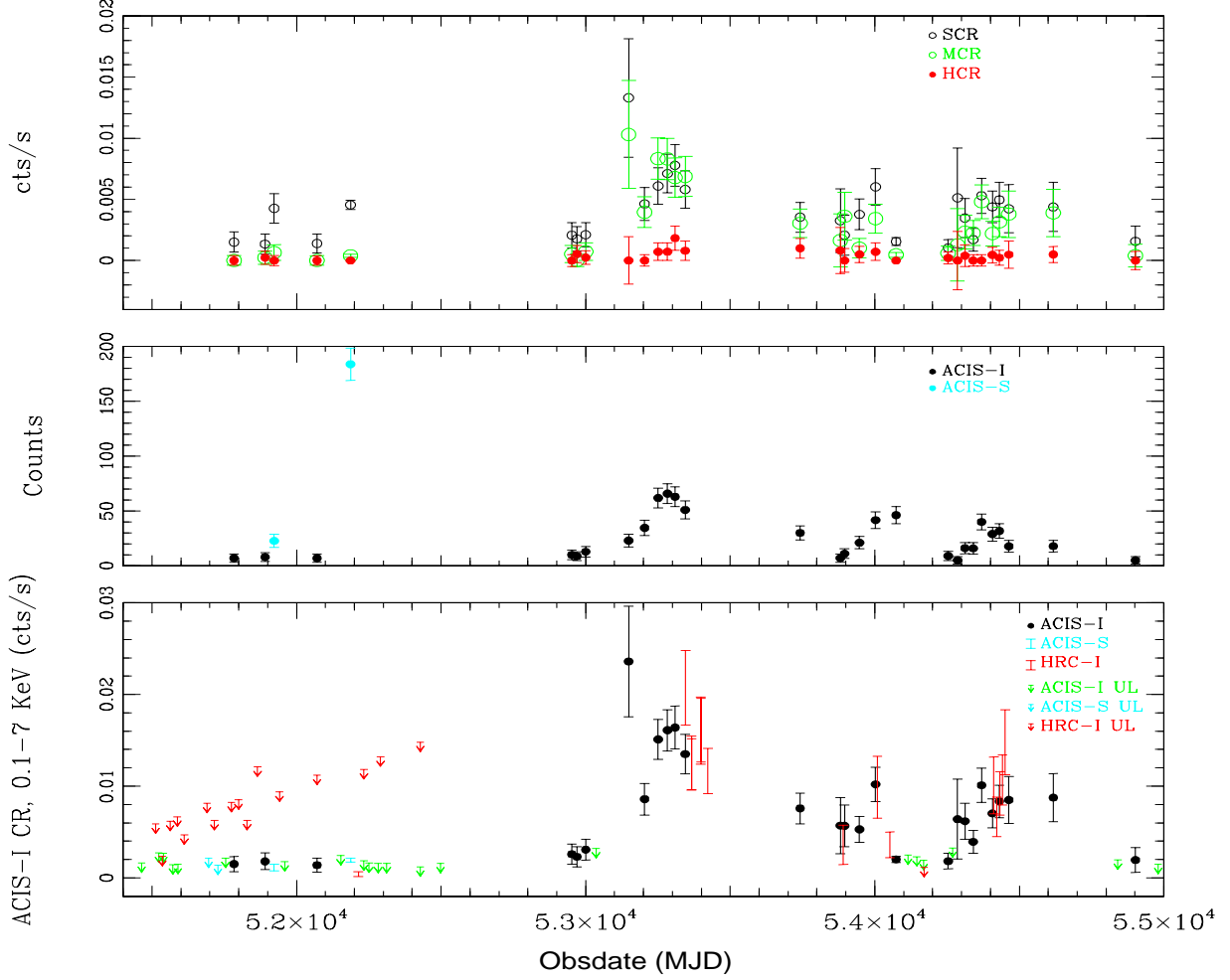


Fig. 3.—: Light curve for r1-25. *Bottom Panel:* Count Rate in the Soft (0.1-1.1 keV), Medium (1.1-2 keV), and Hard (2-7 keV) bands vs. Obsdate. *Middle Panel:* Total counts for ACIS observations of r1-25 vs. Obsdate. *Bottom Panel:* TCR in ACIS-I units (in the energy range of 0.1-7 keV) vs. Obsdate. See text for how we converted ACIS-S and HRC-I observations to ACIS-I units.

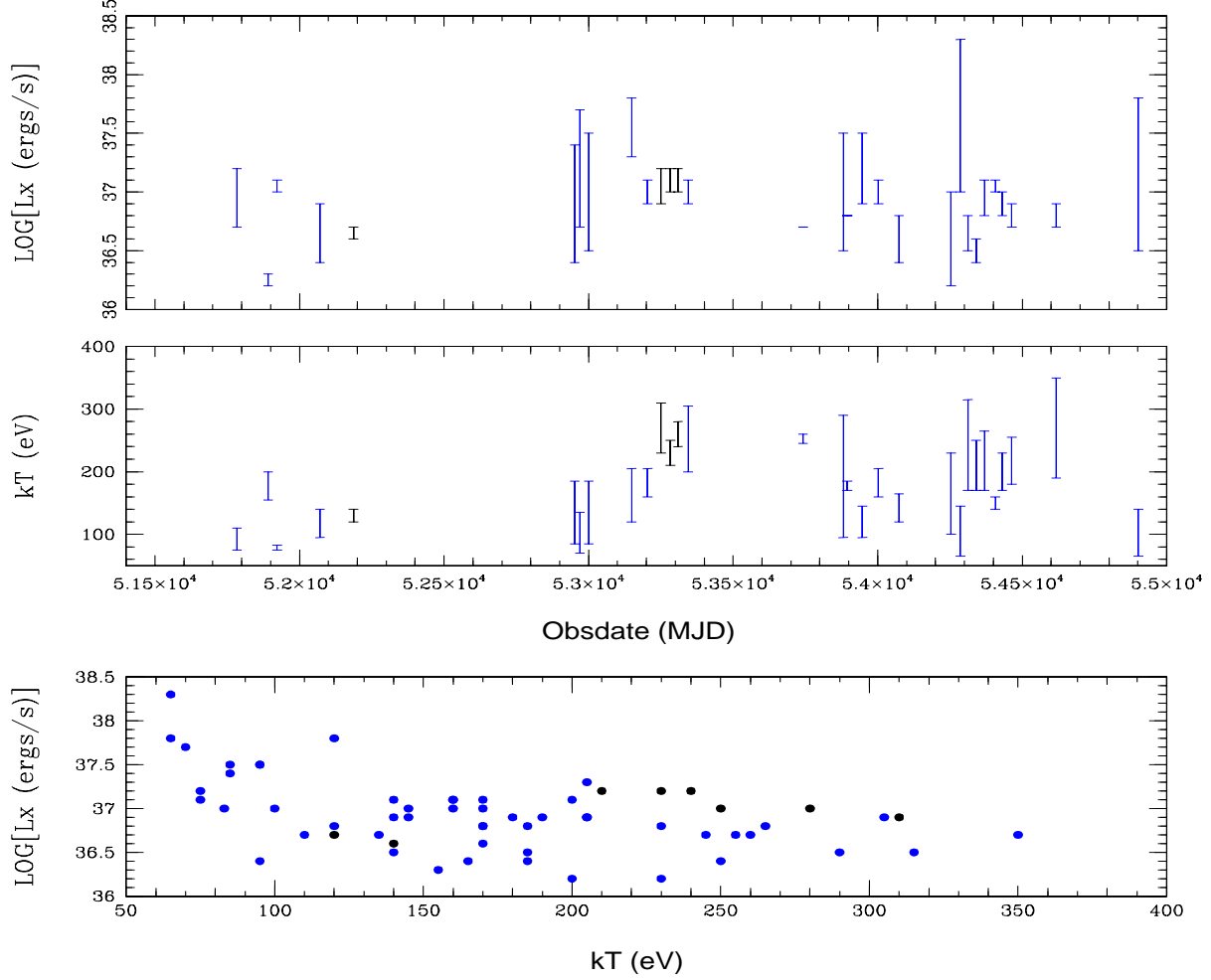


Fig. 4.—: r1-25 spectral analysis. The blue and black symbols represent spectral results from *pimms* and *XSPEC*, respectively. Plots assume $N_H = 1 \times 10^{21} \text{ cm}^{-2}$. *Top Panel:* Plot of logarithm of X-ray luminosity, $\text{LOG}[L_X]$, vs. Obsdate for ACIS observations that detected r1-25 (L_X in the 0.1-7 keV range). *Middle Panel:* Plot of kT vs. Obsdate for ACIS observations that detected r1-25. *Bottom Panel:* Plot of $\text{LOG}[L_X]$ vs. kT .

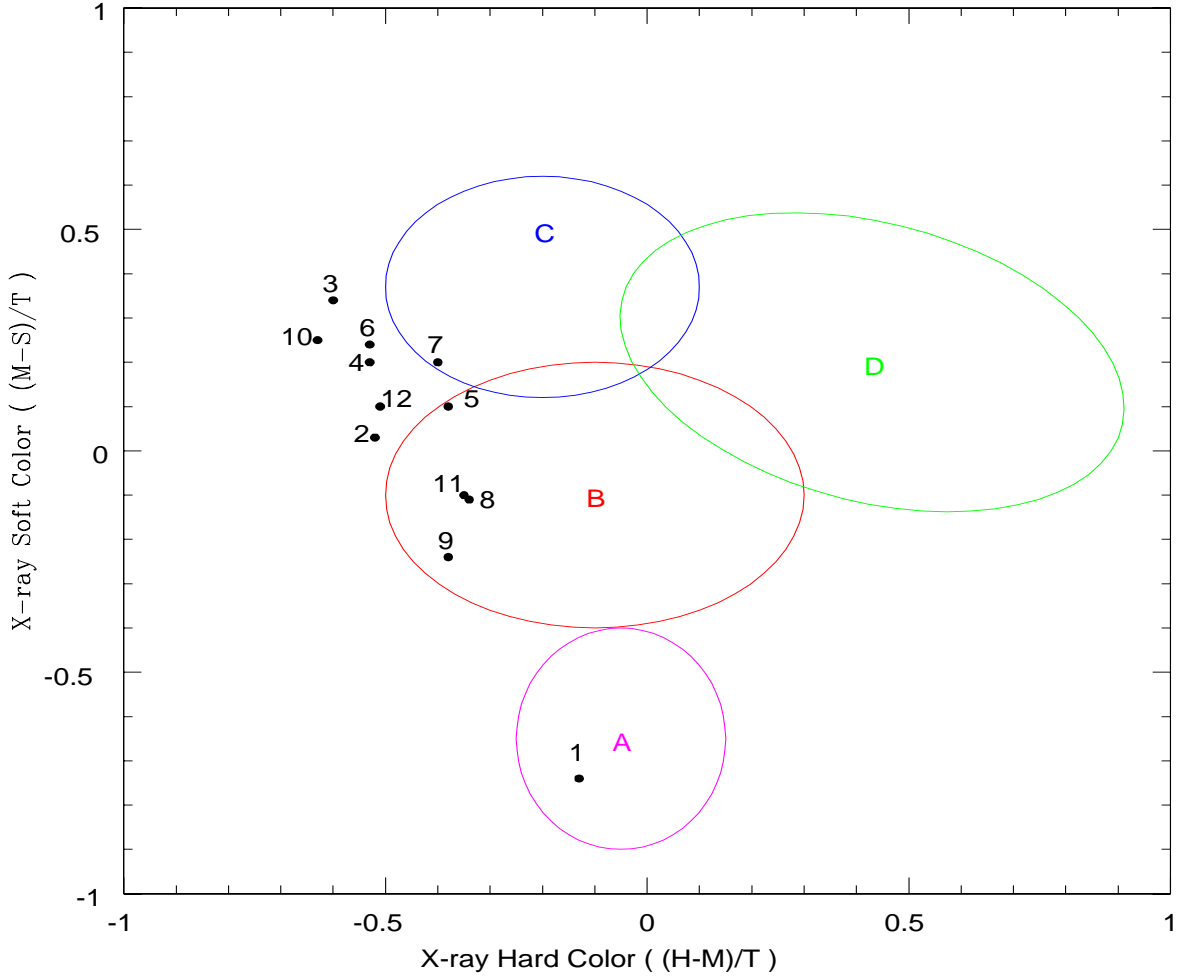


Fig. 5.—: Only detections of r1-25 with 25 or more counts were included on this color-color graph. The numbers refer to the observations in Table 9. The ellipses were taken from Prestwich et al. (2003). Ellipse A is generally associated with SNRs, Ellipse B with LMXBs, Ellipse C with absorbed sources, and Ellipse D with HMXBs. The bands used for this plot were: S,0.3-1 keV; M,1-2 keV; H,2-8 keV; and T,0.3-8 keV.

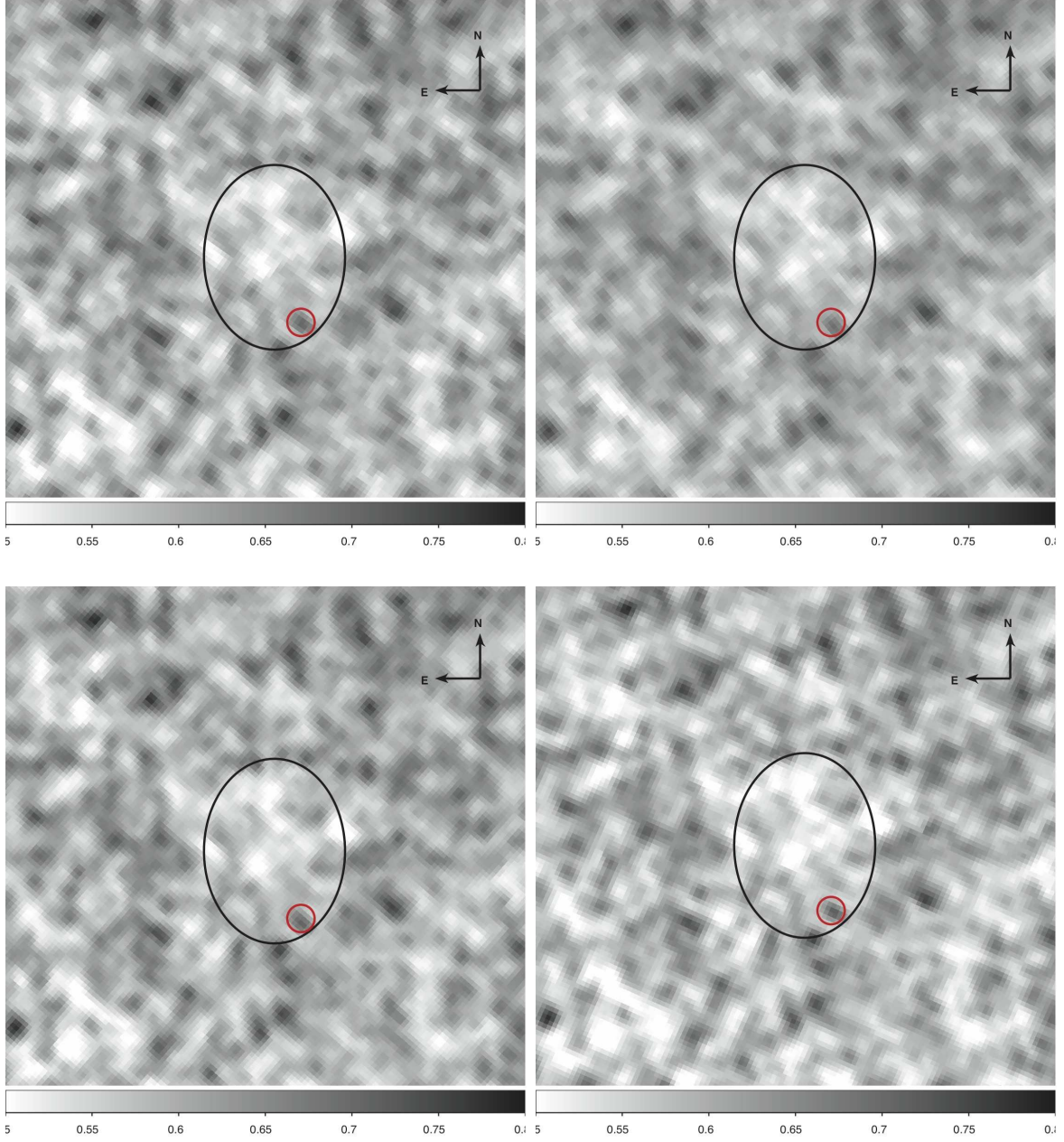


Fig. 6.—: HST ACS images of the location of r1-25, obtained in the F435W filter on four separate dates (see Table 13). *Top Left*: Observation j8vp03010, *Top Right*: observation j8vp05010, *Bottom Left*: Observation j9ju01010, *Bottom Right*: Observation j9ju06010. Each image is $3''$ on a side. The black ellipse denotes the 3σ X-ray positional error ellipse of r1-25. The ellipse has a semi-major axis (3σ RA error) = $0.39''$ and a semi-minor axis (3σ DEC error) = $0.51''$. The red circle shows the only consistently detected, resolved source found by DAOphot.

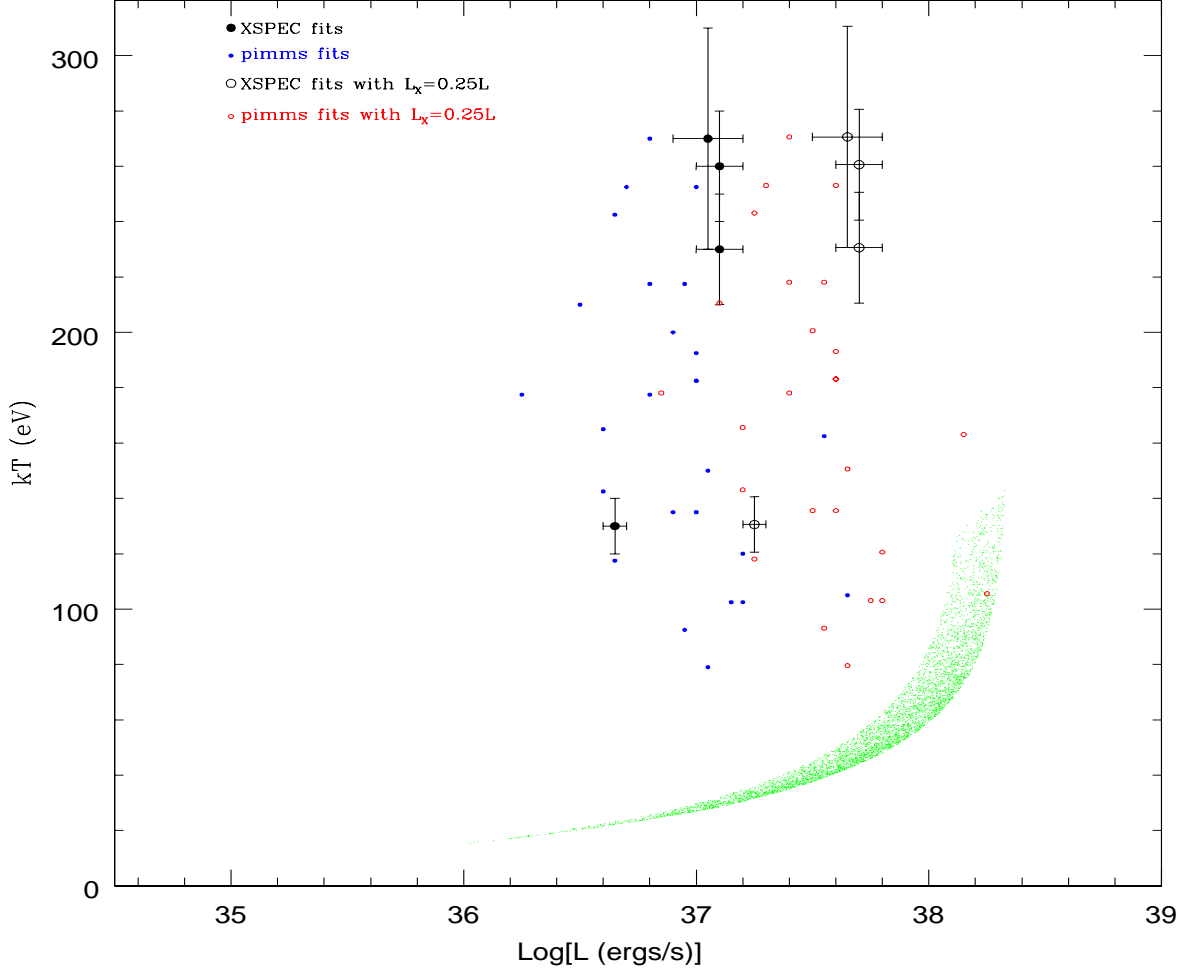


Fig. 7.—: Plot of kT vs. the logarithm of the bolometric luminosity, $\text{LOG}[L]$. The black and blue points are the average kT and $\text{LOG}[L]$ for XSPEC and **pimms** spectral fits of r1-25, respectively (assuming $N_H = 1 \times 10^{21} \text{ cm}^{-2}$). The solid black points represent XSPEC fits assuming $L_X = L$, and the open black points assume $L_X = 0.25L$ for XSPEC fits. The blue points represent the **pimms** results assuming $L_X = L$. The red points correspond to **pimms** results assuming $L_X = L_X = 0.25L$ (see text). The error bars represent the range of kT and L_X that fit each observation with XSPEC results (see Table 8). The error bars are not plotted for the **pimms** points as the uncertainties are too large (see text). The green points represent the kT and $\text{LOG}[L]$ for various quasi-steady nuclear burning white dwarfs.

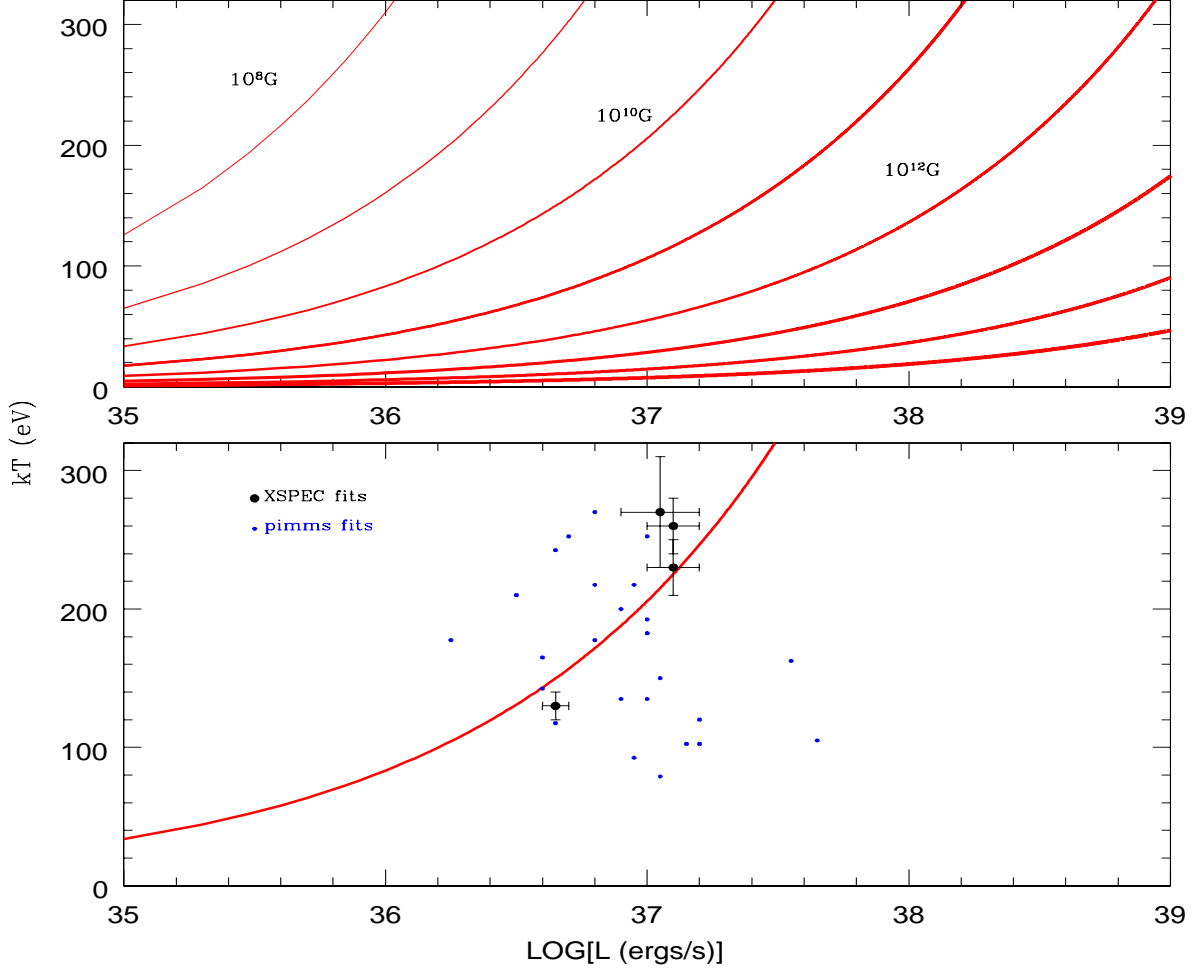


Fig. 8.—: Plot of kT versus L for the neutron star model described by Equation 4. *Top Panel:* Each curve corresponds to a fixed value of the magnetic field on the surface of the neutron star; B_s changes by a factor of ten between curves. Since the field is not expected to vary this much over short times, the system should evolve *along* the curves. Thus, if the luminosity increases or decreases, so does the temperature. *Bottom Panel:* The $B_s = 10^{10} \text{ G}$ curve is plotted with the r1-25 spectra. The black and blue points are the average kT and $\text{LOG}[L]$ for XSPEC and **pimms** spectral fits of r1-25, respectively (assuming $N_H = 1 \times 10^{21} \text{ cm}^{-2}$). The error bars represent the range of kT and L_X that fit each observation (see Table 8). The error bars are not plotted for the **pimms** points as the uncertainties are too large (see text).

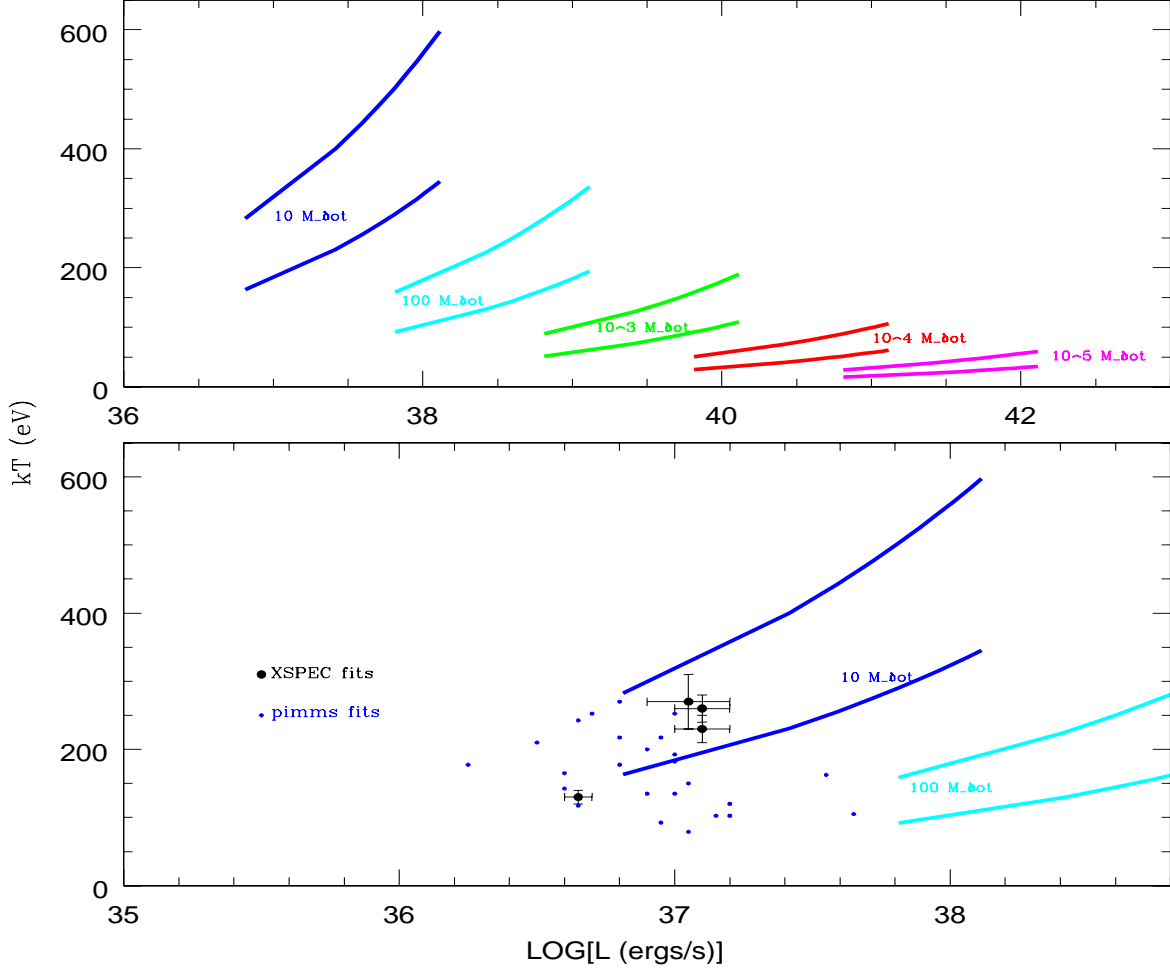


Fig. 9.—: Figure taken from Di Stefano et al. (2010). It is a plot of kT versus $\text{LOG}[L]$ for the inner portion of the accretion disk around black holes. *Top Panel:* Each pair of two curves of a single color corresponds to a fixed black hole mass which labels the regions between the curves. The upper curve of each color corresponds to a disk with inner radius $6M_{BH}G/c^2$, while the lower curve corresponds to an inner disk with 3 times the radius. The point at the bottom (top) of each curve corresponds to the luminosity of the inner disk being $1\%L_{\text{Eddington}}$ ($10\%L_{\text{Eddington}}$). *Bottom Panel:* The $10M_{\odot}$ and $100M_{\odot}$ curves are plotted with the r1-25 spectra. The black and blue points are the average kT and $\text{LOG}[L]$ for XSPEC and *pimms* spectral fits of r1-25, respectively (assuming $N_H = 1 \times 10^{21} \text{ cm}^{-2}$). The error bars represent the range of kT and L_X that fit each observation (see Table 8). The error bars are not plotted for the *pimms* points as the uncertainties are too large (see text).

Table 1. *Chandra* Observations of r1-25

ObsID	Instrument	Exposure Time seconds	Observation Date	OBSMJD	Detected r1-25?
303	ACIS-I	11862	1999-10-13	51464.2	No
267	HRC-I	1270	1999-11-30	51512.8	No
305	ACIS-I	4129	1999-12-11	51523.2	No
268	HRC-I	5178	1999-12-23	51535.1	No
306	ACIS-I	4132	1999-12-27	51539.7	No
269	HRC-I	1206	2000-01-19	51562.9	No
307	ACIS-I	4113	2000-01-29	51572.6	No
270	HRC-I	1470	2000-02-13	51587.2	No
308	ACIS-I	4012	2000-02-16	51590.1	No
271	HRC-I	2464	2000-03-08	51611.8	No
272	HRC-I	1203	2000-05-26	51690.7	No
309	ACIS-S	5089	2000-06-01	51696.1	No
273	HRC-I	1191	2000-06-21	51716.2	No
310	ACIS-S	5074	2000-07-02	51727.9	No
311	ACIS-I	4894	2000-07-29	51754.0	No
275	HRC-I	1188	2000-08-18	51774.4	No
312	ACIS-I	4666	2000-08-27	51783.8	Yes
276	HRC-I	1183	2000-09-11	51798.9	No
277	HRC-I	1187	2000-10-12	51829.2	No
278	HRC-I	1182	2000-11-17	51865.2	No
1581	ACIS-I	4404	2000-12-13	51891.1	Yes
1854	ACIS-S	4694	2001-01-13	51922.4	Yes
1569	HRC-I	1169	2001-02-01	51941.0	No
1582	ACIS-I	4303	2001-02-18	51958.7	No
1583	ACIS-I	4903	2001-06-10	52070.8	Yes
1570	HRC-I	1184	2001-06-10	52070.9	No
1577	ACIS-I	4916	2001-08-31	52152.5	No
1575	ACIS-S	37664	2001-10-05	52187.0	Yes
1912	HRC-I	46732	2001-10-31	52214.0	Yes
1585	ACIS-I	4884	2001-11-19	52232.8	No
2904	HRC-I	1182	2001-11-19	52232.9	No
2895	ACIS-I	4881	2001-12-07	52250.8	No
2897	ACIS-I	4900	2002-01-08	52282.1	No
2905	HRC-I	1094	2002-01-16	52290.2	No
2896	ACIS-I	4903	2002-02-06	52311.9	No
2898	ACIS-I	4900	2002-06-02	52427.9	No
2906	HRC-I	1188	2002-06-02	52427.9	No
4360	ACIS-I	4906	2002-08-11	52497.7	No
4678	ACIS-I	3894	2003-11-09	52952.3	Yes
4679	ACIS-I	3820	2003-11-26	52969.9	Yes
4680	ACIS-I	4198	2003-12-27	53000.3	Yes
4681	ACIS-I	4094	2004-01-31	53035.8	No
4682	ACIS-I	3945	2004-05-23	53148.7	Yes
4719	ACIS-I	4123	2004-07-17	53203.9	Yes
4720	ACIS-I	4108	2004-09-02	53250.6	Yes

Table 1—Continued

ObsID	Instrument	Exposure Time seconds	Observation Date	OBSMJD	Detected r1-25?
4721	ACIS-I	4132	2004-10-04	53282.9	Yes
4722	ACIS-I	3894	2004-10-31	53309.1	Yes
4723	ACIS-I	4035	2004-12-05	53344.4	Yes
5925	HRC-I	46311	2004-12-06	53345.8	Yes
6177	HRC-I	20038	2004-12-27	53366.3	Yes
5926	HRC-I	28268	2004-12-27	53366.8	Yes
6202	HRC-I	18046	2005-01-28	53398.1	Yes
5927	HRC-I	27000	2005-01-28	53398.8	Yes
5928	HRC-I	44856	2005-02-21	53422.7	Yes
7136	ACIS-I	3991	2006-01-06	53741.8	Yes
7137	ACIS-I	3952	2006-05-26	53881.2	Yes
7283	HRC-I	19942	2006-06-05	53891.3	Yes
7138	ACIS-I	4107	2006-06-09	53895.7	Yes
7139	ACIS-I	3987	2006-07-31	53947.0	Yes
7140	ACIS-I	4117	2006-09-24	54002.8	Yes
7284	HRC-I	20002	2006-09-30	54008.9	Yes
7285	HRC-I	18517	2006-11-13	54052.3	Yes
7064	ACIS-I	23238	2006-12-04	54073.9	Yes
8183	ACIS-I	3965	2007-01-14	54114.9	No
8184	ACIS-I	4140	2007-02-14	54145.1	No
8185	ACIS-I	3965	2007-03-10	54169.2	No
7286	HRC-I	18708	2007-03-11	54170.6	No
7068	ACIS-I	7693	2007-06-02	54253.9	Yes
8191	ACIS-I	3959	2007-06-18	54269.3	No
8192	ACIS-I	4073	2007-07-05	54286.5	Yes
8193	ACIS-I	4129	2007-07-31	54312.1	Yes
8194	ACIS-I	4033	2007-08-28	54340.5	Yes
8195	ACIS-I	3965	2007-09-26	54369.6	Yes
8186	ACIS-I	4134	2007-11-03	54407.2	Yes
8526	HRC-I	19944	2007-11-07	54411.6	Yes
8527	HRC-I	19981	2007-11-17	54421.8	Yes
8187	ACIS-I	3837	2007-11-27	54431.2	Yes
8528	HRC-I	19975	2007-11-28	54432.8	Yes
8529	HRC-I	18923	2007-12-07	54441.6	Yes
8530	HRC-I	19915	2007-12-17	54451.5	Yes
9529	ACIS-I	4113	2008-05-31	54617.5	Yes
9520	ACIS-I	3962	2008-12-31	54463.7	Yes
10551	ACIS-I	3965	2009-01-09	54841.0	No
10552	ACIS-I	3962	2009-02-07	54869.4	No
10553	ACIS-I	4104	2009-03-11	54901.6	Yes
10554	ACIS-I	4036	2009-05-29	54980.1	No

Table 2. Photometry for r1-25

OBSMJD	Soft Counts	Medium Counts	Hard Counts	Total Counts	SCR 10^{-3}s^{-1}	MCR 10^{-3}s^{-1}	HCR 10^{-3}s^{-1}	TCR 10^{-3}s^{-1}	ACIS-I Rate 10^{-3}s^{-1}
51464.2	< 1.63	< 1.63
51512.8	< 4.66	< 5.87
51523.2	< 2.70	< 2.70
51535.1	< 1.85	< 2.33
51539.7	< 2.70	< 2.70
51562.9	< 4.90	< 6.17
51572.6	< 1.44	< 1.44
51587.2	< 5.29	< 6.66
51590.1	< 1.47	< 1.47
51611.8	< 3.73	< 4.70
51690.7	< 6.46	< 8.13
51696.1	< 4.20	< 2.17
51716.2	< 4.97	< 6.26
51727.9	< 2.71	< 1.40
51754.0	< 2.16	< 2.16
51774.4	< 6.53	< 8.22
51783.8	6.92 \pm 3.80	0.00 \pm 1.87	0.00 \pm 1.87	6.92 \pm 3.79	1.50 \pm 0.82	0.00 \pm 0.41	0.00 \pm 0.41	1.50 \pm 0.82	1.50 \pm 0.82
51798.9	< 6.76	< 8.51
51829.2	< 4.98	< 6.27
51865.2	< 9.57	< 12.05
51891.1	5.83 \pm 3.60	1.00 \pm 2.32	1.00 \pm 2.32	7.83 \pm 3.96	1.34 \pm 0.83	0.23 \pm 0.53	0.23 \pm 0.53	1.80 \pm 0.91	1.80 \pm 0.91
51922.4	19.75 \pm 5.56	3.00 \pm 2.94	0.00 \pm 1.91	22.66 \pm 5.88	4.26 \pm 1.20	0.65 \pm 0.63	0.00 \pm 0.41	4.89 \pm 1.27	0.79-1.48
51941.0	< 7.97	< 9.36
51958.7	< 1.79	< 1.79
52070.8	6.75 \pm 3.79	0.00 \pm 1.87	0.00 \pm 1.87	6.75 \pm 3.79	1.39 \pm 0.78	0.00 \pm 0.38	0.00 \pm 0.38	1.39 \pm 0.78	1.39 \pm 0.78
52070.9	< 9.56	< 11.22
52152.5	< 2.45	< 2.45
52187.0	169.67 \pm 14.15	14.33 \pm 4.98	0.00 \pm 1.88	183.75 \pm 14.71	4.55 \pm 0.38	0.38 \pm 0.13	0.00 \pm 0.05	4.92 \pm 0.39	1.71-2.14
52214.0	0.46 \pm 0.13	0.147-0.686
52232.8	< 1.86	< 1.86
52232.9	< 6.50	< 11.76
52250.8	< 1.61	< 1.61
52282.1	< 1.59	< 1.59
52290.2	< 7.30	< 13.21
52311.9	< 1.59	< 1.59
52427.9	< 1.21	< 1.21
52427.9	< 8.19	< 14.82
52497.7	< 1.58	< 1.58
52952.3	7.92 \pm 3.96	2.00 \pm 2.66	0.00 \pm 1.87	9.92 \pm 4.28	2.06 \pm 1.03	0.52 \pm 0.69	0.00 \pm 0.49	2.58 \pm 1.11	2.58 \pm 1.11
52969.9	6.67 \pm 3.79	0.00 \pm 1.87	2.00 \pm 2.66	8.67 \pm 4.13	1.77 \pm 1.01	0.00 \pm 0.50	0.53 \pm 0.71	2.30 \pm 1.10	2.30 \pm 1.10
53000.3	8.75 \pm 4.13	3.00 \pm 2.94	1.00 \pm 2.32	12.75 \pm 4.71	2.11 \pm 0.99	0.72 \pm 0.71	0.24 \pm 0.56	3.07 \pm 1.13	3.07 \pm 1.13
53035.8	< 3.22	< 3.22
53148.7	12.92 \pm 4.71	10.00 \pm 4.28	0.00 \pm 1.87	22.92 \pm 5.87	13.31 \pm 4.85	10.30 \pm 4.41	0.00 \pm 1.93	23.62 \pm 6.05	23.62 \pm 6.05
53203.9	18.67 \pm 5.45	15.92 \pm 5.09	0.00 \pm 1.87	34.58 \pm 6.98	4.63 \pm 1.35	3.95 \pm 1.26	0.00 \pm 0.46	8.58 \pm 1.73	8.58 \pm 1.73
53250.6	24.92 \pm 6.08	34.00 \pm 6.89	2.92 \pm 2.94	61.83 \pm 8.92	6.10 \pm 1.49	8.33 \pm 1.69	0.72 \pm 0.72	15.14 \pm 2.18	15.14 \pm 2.18
53282.9	29.00 \pm 6.45	33.83 \pm 6.90	2.92 \pm 2.94	65.75 \pm 9.17	7.11 \pm 1.58	8.30 \pm 1.69	0.72 \pm 0.72	16.12 \pm 2.25	16.12 \pm 2.25
53309.1	29.83 \pm 6.55	26.00 \pm 6.17	7.00 \pm 3.78	62.83 \pm 8.99	7.78 \pm 1.71	6.78 \pm 1.61	1.83 \pm 0.99	16.38 \pm 2.34	16.38 \pm 2.34
53344.4	21.92 \pm 5.77	25.92 \pm 6.17	3.00 \pm 2.94	50.83 \pm 8.19	5.81 \pm 1.53	6.87 \pm 1.64	0.80 \pm 0.78	13.47 \pm 2.17	13.47 \pm 2.17
53345.8	14.63 \pm 0.57	16.70-24.85
53366.3	8.78 \pm 0.67	9.59-15.45
53366.8	8.72 \pm 0.57	9.65-15.19
53398.1	11.31 \pm 0.80	12.44-19.78
53398.8	11.35 \pm 0.66	12.67-19.62
53422.7	8.23 \pm 0.44	9.23-14.16
53741.8	14.00 \pm 4.84	12.00 \pm 4.57	3.92 \pm 3.18	29.92 \pm 6.55	3.54 \pm 1.22	3.04 \pm 1.16	0.99 \pm 0.80	7.57 \pm 1.66	7.57 \pm 1.66
53881.2	4.00 \pm 3.18	2.00 \pm 2.66	1.00 \pm 2.32	7.00 \pm 3.78	3.26 \pm 2.59	1.63 \pm 2.17	0.81 \pm 1.89	5.70 \pm 3.08	5.70 \pm 3.08
53891.3	3.35 \pm 0.43	1.46-5.76
53895.7	4.00 \pm 3.18	7.00 \pm 3.78	0.00 \pm 1.87	11.00 \pm 4.43	2.06 \pm 1.64	3.61 \pm 1.95	0.00 \pm 0.96	5.67 \pm 2.28	5.67 \pm 2.28
53947.0	15.00 \pm 4.97	4.00 \pm 3.18	2.00 \pm 2.66	21.00 \pm 5.66	3.77 \pm 1.25	1.01 \pm 0.80	0.50 \pm 0.67	5.28 \pm 1.42	5.28 \pm 1.42
54002.8	24.67 \pm 6.08	14.00 \pm 4.84	2.92 \pm 2.94	41.58 \pm 7.58	6.02 \pm 1.48	3.42 \pm 1.18	0.71 \pm 0.72	10.15 \pm 1.85	10.15 \pm 1.85
54008.9	10.64 \pm 0.74	6.52-13.24
54052.3	3.83 \pm 0.47	2.22-5.00
54073.9	35.50 \pm 7.07	10.75 \pm 4.43	0.00 \pm 1.87	46.08 \pm 7.92	1.55 \pm 0.31	0.47 \pm 0.19	0.00 \pm 0.08	2.01 \pm 0.34	2.01 \pm 0.34
54114.9	< 2.49	< 2.49
54145.1	< 2.32	< 2.32
54169.2	< 1.92	< 1.92

Table 2—Continued

OBSMJD	Soft Counts	Medium Counts	Hard Counts	Total Counts	SCR 10^{-3}s^{-1}	MCR 10^{-3}s^{-1}	HCR 10^{-3}s^{-1}	TCR 10^{-3}s^{-1}	ACIS-I Rate 10^{-3}s^{-1}
54170.6	< 0.88	< 1.13
54253.9	5.00 ± 3.40	2.92 ± 2.94	1.00 ± 2.32	8.92 ± 4.12	1.02 ± 0.69	0.59 ± 0.60	0.20 ± 0.47	1.82 ± 0.84	1.82 ± 0.84
54269.3	< 3.28	< 3.28
54286.5	4.00 ± 3.18	1.00 ± 2.32	0.00 ± 1.87	5.00 ± 3.40	5.12 ± 4.07	1.28 ± 2.97	0.00 ± 2.39	6.40 ± 4.35	6.40 ± 4.35
54312.1	9.00 ± 4.12	6.00 ± 3.60	1.00 ± 2.32	16.00 ± 5.09	3.47 ± 1.59	2.32 ± 1.39	0.39 ± 0.90	6.18 ± 1.96	6.18 ± 1.96
54340.5	6.83 ± 3.79	9.00 ± 4.12	0.00 ± 1.87	15.83 ± 5.09	1.70 ± 0.94	2.24 ± 1.02	0.00 ± 0.46	3.93 ± 1.26	3.93 ± 1.26
54369.6	20.92 ± 5.66	19.00 ± 5.44	0.00 ± 1.87	39.92 ± 7.38	5.29 ± 1.43	4.81 ± 1.38	0.00 ± 0.47	10.10 ± 1.87	10.10 ± 1.87
54407.2	18.00 ± 5.33	9.00 ± 4.12	1.83 ± 2.66	28.83 ± 6.46	4.39 ± 1.30	2.20 ± 1.01	0.45 ± 0.65	7.03 ± 1.58	7.03 ± 1.58
54411.6	9.58 ± 0.71	$6.97\text{--}13.19$
54421.8	6.30 ± 0.58	$4.45\text{--}8.81$
54431.2	18.83 ± 5.45	12.00 ± 4.57	0.83 ± 2.33	31.67 ± 6.73	4.96 ± 1.44	3.16 ± 1.20	0.22 ± 0.61	8.34 ± 1.77	8.34 ± 1.77
54432.8	7.69 ± 0.63	$6.84\text{--}11.57$
54441.6	8.93 ± 0.70	$7.96\text{--}13.39$
54451.5	12.39 ± 0.80	$11.23\text{--}18.35$
54463.7	8.83 ± 4.12	7.92 ± 3.96	1.00 ± 2.32	17.75 ± 5.33	4.23 ± 1.97	3.79 ± 1.90	0.48 ± 1.11	8.50 ± 2.55	8.50 ± 2.55
54617.5	8.92 ± 4.12	7.92 ± 3.96	1.00 ± 1.32	17.83 ± 5.33	4.38 ± 2.02	3.89 ± 1.94	0.49 ± 0.65	8.75 ± 2.62	8.75 ± 2.62
54841.0	< 1.96	< 1.96
54869.4 ^a	... ^a
54901.6	3.92 ± 3.18	1.00 ± 2.32	0.00 ± 1.87	4.92 ± 3.40	1.56 ± 1.26	0.40 ± 0.92	0.00 ± 0.74	1.95 ± 1.35	1.95 ± 1.35
54980.1	< 1.50	< 1.50

Note. — Columns 2, 3, and 4 are the counts in the Soft (0.1–1.1 keV), Medium (1.1–2 keV), and Hard (2–7 keV) bands, respectively. The fourth column is Total Counts for ACIS observations (in the energy range of 0.1–7 keV). The next four columns are Soft, Medium, Hard, and Total count rates, respectively. All rates are corrected by a vignetting factor. The last column is the TCR converted into units of ACIS-I Count Rate, in the energy range of 0.1–7 keV (see text).

^aNo upper limit could be calculated for r1-25 in this observation, as there were zero counts in both the source and background apertures.

Table 3. Spectral Fitting Results

Obs ID	kT (keV)	$N_H = 1 \times 10^{21} \text{ cm}^{-2}$		kT (keV)	$N_H = 6.4 \times 10^{21} \text{ cm}^{-2}$	
		Normalization	L_X ($10^{37} \text{ ergs s}^{-1}$)		Normalization (10^{-6})	L_X ($10^{37} \text{ ergs s}^{-1}$)
1575	0.13 ± 0.01	$0.76^{+0.7}_{-0.8}$	0.4	0.08 ± 0.002	$8.0^{+1.2}_{-1.1}$	19.7
4720	0.27 ± 0.04	$1.8^{+0.2}_{-0.3}$	1.0	0.19 ± 0.02	$7.8^{+2.6}_{-1.6}$	4.2
4721	0.23 ± 0.02	$2.1^{+0.3}_{-0.3}$	1.1	0.16 ± 0.01	$14.0^{+5.2}_{-3.4}$	6.8
4722	0.26 ± 0.02	$2.0^{+0.3}_{-0.3}$	1.1	$0.15^{+0.04}_{-0.01}$	$19.8^{+9.8}_{-9.8}$	9.1

Note. — Spectral fits were carried out in the energy range 0.3–8.0 keV. Luminosities are given for the same energy range and are corrected for assumed absorption. All quoted uncertainties are 1σ .

Table 4. Results of spectral simulations

Sim obs ID	Orig obs ID	N_H (10^{21} cm $^{-2}$)	SCR	MCR	HCR	TCR
4720	1575	1.1	5.87 ± 2.42	1.30 ± 1.14	0.00 ± 0.04	7.17 ± 2.72
4720	1575	6.4	7.62 ± 2.65	0.99 ± 1.01	0.00 ± 0.00	8.60 ± 2.85
4721	1575	1.1	5.89 ± 2.44	1.20 ± 1.09	0.00 ± 0.05	7.09 ± 2.70
4721	1575	6.4	7.51 ± 2.70	0.95 ± 0.94	0.00 ± 0.03	8.46 ± 2.89
4722	1575	1.1	5.49 ± 2.47	1.20 ± 1.10	0.00 ± 0.06	6.70 ± 2.67
4722	1575	6.4	7.24 ± 2.68	0.92 ± 0.95	0.00 ± 0.00	8.16 ± 2.81
1575	4720	1.1	542.89 ± 23.59	459.62 ± 21.86	33.21 ± 5.65	1035.72 ± 32.17
1575	4720	6.4	357.65 ± 19.76	472.02 ± 21.16	12.38 ± 3.66	842.05 ± 30.02
1575	4721	1.1	720.86 ± 26.35	430.37 ± 20.03	17.61 ± 4.13	1168.83 ± 33.24
1575	4721	6.4	531.22 ± 22.64	484.71 ± 22.07	6.41 ± 2.55	1022.33 ± 31.11
1575	4722	1.1	655.97 ± 26.10	484.68 ± 22.16	27.87 ± 5.10	1168.53 ± 35.45
1575	4722	6.4	618.62 ± 24.65	477.95 ± 22.10	4.58 ± 2.14	1101.15 ± 32.47

Note. — Col (1): Obs ID from which response files were taken from observation. Col. (2): Obs ID of model used for simulation (see Table 3). Col. (3): N_H value simulated. Cols (4),(5) and (6): Simulated total counts and associated 1σ errors.

Table 5. `pimms` Method of Spectral Fitting for r1-25 in ACIS-S Observation 1854

kT keV	$\frac{SCR_p}{TCR_p}$	$\frac{MCR_p}{TCR_p}$	$\frac{HCR_p}{TCR_p}$	$L_{X,p}$ ergs s ⁻¹
0.025	1.00E+00	4.55E-12	0.00E+00	2.09E+39
0.034	1.00E+00	1.91E-08	1.58E-19	3.75E+38
0.045	1.00E+00	6.50E-06	5.13E-14	8.15E+37
0.061	1.00E+00	3.70E-04	4.50E-10	2.37E+37
0.083	9.94E-01	5.99E-03	2.94E-07	9.28E+36
0.112	9.60E-01	4.00E-02	3.04E-05	4.62E+36
0.151	8.64E-01	1.35E-01	7.55E-04	2.84E+36
0.203	7.08E-01	2.85E-01	6.91E-03	2.09E+36
0.274	5.32E-01	4.35E-01	3.29E-02	1.81E+36
0.370	3.78E-01	5.24E-01	9.79E-02	1.82E+36
0.499	2.61E-01	5.30E-01	2.09E-01	2.09E+36
0.673	1.77E-01	4.70E-01	3.53E-01	2.62E+36
0.908	1.19E-01	3.83E-01	4.99E-01	3.52E+36
1.224	8.20E-02	3.01E-01	6.17E-01	4.97E+36

Note. — The spectral analysis in this table demonstrates the initial `pimms` method. We input various values of kT (shown in Column 1) into `pimms` (assuming $N_H = 1.1 \times 10^{21}$ cm⁻²) and calculated the ratios of the band count rates (shown in Columns 2-4). The last column shows the `pimms` prediction for the X-ray luminosity (see text). To determine which, if any, of these temperatures fit the source, we compare the `pimms` ratios to the observed ones. The observed ratios for this source are: $0.626 < \frac{SCR}{TCR} < 1.12$, $2.65 \times 10^{-3} < \frac{MCR}{TCR} < 0.262$, $-8.43 \times 10^{-2} < \frac{HCR}{TCR} < 8.43 \times 10^{-2}$. The rows in bold are the models that fit the source in this observation. The range of kT that fit was further reduced by breaking the soft band into smaller bins (see text).

Table 6. Binned Soft Band for r1-25

ObsID	MJD	0.1-0.3 keV	0.3-0.5 keV	0.5-0.7 keV	0.7-0.9 keV	0.9-1.1 keV
312	51783.8	0	2	2	3	0
1581	51891.1	0	0	0	3	3
1854	51922.4	2	8	4	5	1
1583	52070.8	0	0	1	4	2
1575	52187	5	34	60	46	27
4678	52952.3	0	0	2	4	2
4679	52969.9	0	0	3	1	3
4680	53000.3	0	1	0	5	3
4682	53148.7	0	0	2	6	5
4719	53203.9	0	2	4	7	6
4720	53250.6	0	0	7	8	10
4721	53282.9	0	1	10	9	9
4722	53309.1	0	2	8	14	6
4723	53344.4	0	0	9	6	7
7136	53741.8	0	0	1	6	7
7137	53881.2	0	0	1	2	1
7138	53895.7	0	1	1	1	1
7139	53947.0	0	2	1	6	6
7140	54002.8	0	2	7	10	6
7064	54073.9	0	2	7	13	14
7068	54253.9	0	0	1	3	1
8192	54286.5	0	0	2	1	1
8193	54312.1	0	2	1	3	3
8194	54340.5	0	0	1	4	2
8195	54369.6	0	1	3	8	9
8186	54407.2	0	2	4	5	7
8187	54431.2	0	2	5	5	7
9520	54463.7	0	1	2	3	3
9529	54617.5	0	2	3	3	1
10553	54901.6	0	1	0	2	1

Note. — Columns 3-7 are the raw counts in the 0.1-0.3, 0.3-0.5, 0.5-0.7, 0.7-0.9, and 0.9-1.1 keV bands, respectively.

Table 7. Comparison of Results From XSPEC and **pimms**

OBS ID	OBSMJD	XSPEC kT (eV)	pimms kT (eV)
1575	52187.0	120 - 140	120 - 135
4720	53250.6	230 - 310	220 - 300
4721	53282.9	210 - 250	205 - 290
4722	53309.1	240 - 280	No Fit

Note. — Results are for $N_H = 1.1 \times 10^{21} \text{ cm}^{-2}$. The kT range for XSPEC are based on 1σ uncertainties. For ObsID 4722, **pimms** was unable to determine a black body fit.

Table 8. r1-25 Spectrum

ObsID	OBSMJD	kT (eV)	LOG[L _X (ergs s ⁻¹)]
312	51783.8	75 - 110	36.66 - 37.24
1581	51891.1	155 - 200	36.20 - 36.32
1854	51922.4	75 - 83	36.96 - 37.09
1583	52070.8	95 - 140	36.35 - 36.89
1575 ^a	52187.0	120 - 140	36.64 - 36.69
4678	52952.3	85 - 185	36.44 - 37.40
4679	52969.9	70 - 135	36.67 - 37.71
4680	53000.3	85 - 185	36.49 - 37.48
4682	53148.7	120 - 205	37.31 - 37.83
4719	53203.9	160 - 205	36.87 - 37.06
4720 ^a	53250.6	230 - 310	36.90 - 37.20
4721 ^a	53282.9	210 - 250	37.00 - 37.20
4722 ^a	53309.1	240 - 280	37.00 - 37.20
4723	53344.4	200 - 305	36.90 - 37.08
7136	53741.8	245 - 260	36.71 - 36.72
7137	53881.2	95 - 290	36.54 - 37.54
7138	53895.7	175 - 185	36.76 - 36.83
7139	53947.0	95 - 145	36.95 - 37.50
7140	54002.8	160 - 205	36.94 - 37.14
7064	54073.9	120 - 165	36.40 - 36.75
7068	54253.9	100 - 230	36.17 - 36.96
8192	54286.5	65 - 145	37.01 - 38.25
8193	54312.1	170 - 315	36.54 - 36.84
8194	54340.5	170 - 250	36.40 - 36.64
8195	54369.6	170 - 265	36.79 - 37.05
8186	54407.2	140 - 160	36.95 - 37.09
8187	54431.2	170 - 230	36.77 - 36.97
9520	54463.7	180 - 255	36.73 - 36.93
9529	54617.5	190 - 350	36.68 - 36.90
10553	54901.6	65 - 140	36.55 - 37.76

Note. — Results are for $N_H = 1.1 \times 10^{21} \text{ cm}^{-2}$. The minimum kT corresponds to the maximum luminosity for all r1-25 observations. L_X is in the 0.1-7 keV range. See text for how the kT and L_X were calculated.

^aThe spectra for these observations are from XSPEC fits (see text). The L_X for these observations were converted to the 0.1-7 keV range for consistency.

Table 9. r1-25 Color Ratios

Detection Number	OBSMJD	Hard Color ((H-M)/T)	Soft Color ((M-S)/T)
1	52187.0	-0.13	-0.74
2	53203.9	-0.52	0.03
3	53250.6	-0.60	0.34
4	53282.9	-0.53	0.20
5	53309.1	-0.38	0.10
6	53344.4	-0.53	0.24
7	53741.8	-0.40	0.20
8	54002.8	-0.34	-0.11
9	54073.9	-0.38	-0.24
10	54369.6	-0.63	0.25
11	54407.2	-0.35	-0.10
12	54431.2	-0.51	0.10

Note. — The numbers in the first column correspond to the points plotted in Figure 5. Bands used for these ratios were: S:0.3-1 keV, M:1-2 keV, H:2-8 keV, and T:0.3-8 keV. See text for how the Hard and Soft ratios were calculated.

Table 10. ACS Observations of r1-25

Date	Dataset	Filter	Exposure Time (s)
2004-01-23 07:14:05	j8vp03010	F435W	2200
2004-08-15 00:19:24	j8vp05010	F435W	2200
2006-02-10 03:58:08	j9ju01010	F435W	4360
2007-01-10 23:06:03	j9ju06010	F435W	4672